REPORT DOCUMENTATION PAGE	Form Approved OMB NO. 0704-0188

1. REPORT DATE (DD-MM-YYYY) 23-09-2022	2. REPORT TYPE Thesis or Dissertation	3. DATES COVERED (From - To) -

4. TITLE AND SUBTITLE Characterization of Magic-angle Twisted Bilayer Graphene using Microwave Techniques	5a. CONTRACT NUMBER W911NF-18-1-0116
	5b. GRANT NUMBER
	5c. PROGRAM ELEMENT NUMBER
6. AUTHORS Thao Dinh	5d. PROJECT NUMBER
	5e. TASK NUMBER
	5f. WORK UNIT NUMBER

7. PERFORMING ORGANIZATION NAMES AND ADDRESSES Massachusetts Institute of Technology (MIT 77 Massachusetts Avenue NE18-901 Cambridge, MA 02139 -4307	8. PERFORMING ORGANIZATION REPORT NUMBER
9. SPONSORING/MONITORING AGENCY NAME(S) AND ADDRESS (ES) U.S. Army Research Office P.O. Box 12211 Research Triangle Park, NC 27709-2211	10. SPONSOR/MONITOR'S ACRONYM(S) ARO
	11. SPONSOR/MONITOR'S REPORT NUMBER(S) 71720-PE-OC.8

12. DISTRIBUTION AVAILIBILITY STATEMENT

Approved for public release; distribution is unlimited

13. SUPPLEMENTARY NOTES

The views, opinions and/or findings contained in this report are those of the author(s) and should not contrued as an official Department of the Army position, policy or decision, unless so designated by other documentation.

14. ABSTRACT

15. SUBJECT TERMS

16. SECURITY CLASSIFICATION OF:			17. LIMITATION OF ABSTRACT	15. NUMBER OF PAGES	19a. NAME OF RESPONSIBLE PERSON
a. REPORT	b. ABSTRACT	c. THIS PAGE			William Oliver
UU	UU	UU	UU		19b. TELEPHONE NUMBER 617-258-6018

Standard Form 298 (Rev 8/98)
Prescribed by ANSI Std. Z39.18

REPORT DOCUMENTATION PAGE (SF298)
(Continuation Sheet)

Continuation for Block 13

Proposal/Report Number: 71720.8-PE-QC

Report Title: Characterization of Magic-angle Twisted Bilayer Graphene using Microwave Techniques
Report Type: Ph.D. Dissertation

Publication Type: Thesis or Dissertation
Institution: Dept. of Physics, MIT
Date Received: 23-Sep-2022 Completion Date: 5/14/21 5:10PM
Title: Characterization of Magic-angle Twisted Bilayer Graphene using Microwave Techniques
Authors: Thao Dinh
Acknowledged Federal Support: **N**

Characterization of Magic-angle Twisted Bilayer Graphene using Microwave Techniques

by

Thao H. Dinh

Submitted to the Department of Physics
in partial fulfillment of the requirements for the degree of

Bachelor of Science in Physics

at the

MASSACHUSETTS INSTITUTE OF TECHNOLOGY

May 2021

Author . . . .
Department of Physics
May 14, 2021

Certified by . . . .
William D. Oliver
Professor of Electrical Engineering and Computer Science
Thesis Supervisor

Accepted by . . . .
Professor Deepto Chakrabarty
Physics Associate Head, Department of Physics

Characterization of Magic-angle Twisted Bilayer Graphene using Microwave Techniques

by

Thao H. Dinh

Submitted to the Department of Physics
on May 14, 2021, in partial fulfillment of the
requirements for the degree of
Bachelor of Science in Physics

Abstract

Magic-angle twisted bilayer graphene (MATBG) is a highly tunable material platform that exhibits a wide range of novel phases, including correlated insulating states and unconventional superconductivity. Its tunability and potentially high kinetic inductance in the superconducting state are desirable properties for high-coherence, small-form-factor superconducting qubits. This thesis presents a promising experimental method to characterize MATBG in the gigahertz-frequency regime, the operating regime of superconducting qubits. A hybrid on-chip DC-microwave circuit, which integrates a DC four-probe measurement and microwave resonator readout functionalities, enables the investigation of DC transport response and microwave response in the same twisted bilayer graphene device. By measuring the frequency shift of a standard Aluminum coplanar waveguide resonator terminated by a twisted bilayer graphene device, we can extract the contribution of the twisted bilayer graphene inductance. We expect that the experimental method can be utilized to measure MATBG kinetic inductance and superfluid density in a non-invasive manner. This experiment will also be a crucial step towards realizing MATBG-based superconducting qubit circuits.

Thesis Supervisor: William D. Oliver
Title: Professor of Electrical Engineering and Computer Science

Acknowledgments

I would like to express my gratitude for the companionship of many incredible people who have made my undergraduate journey at MIT so meaningful. First and foremost, I would like to thank Prof. William D. Oliver for offering me the opportunity to join the EQuS team and giving me guidance during the one and a half years I spent in the group. I would also like to thank my mentor, Dr. Joel Wang from EQuS, and my collaborator/mentor, Daniel Rodan-Legrain from Jarillo-Herrero's group, for always being patient, supportive, and generous with their time. Their passion for the research area has constantly inspired me, and this thesis would have been impossible without their encouragement and guidance along the way. I would like to acknowledge David Kim and other collaborators at MIT Lincoln laboratory for helping me with microwave-circuit fabrication and device packaging. It has also been an honor for me to work along with other talented and passionate EQuS members. I am grateful for how welcoming and helpful they have been since I joined the group. Lastly, I would like to thank my parents, my academic advisor, Prof. Krishna Rajagopal, and all my friends at home and at MIT for constantly being by my side, giving me wise advice, and encouraging me to pursue my passion.

Contents

List of Figures

Chapter 1

Introduction

1.1 Motivation

Superconducting qubits are currently one of the leading candidates for building near-term, small-scale quantum computers, due in part to several advantages they have over other qubit platforms: lithographic scalability, controllability, nanosecond-scale operability, and relatively long coherence times. Despite several remarkable advances since the initial appearance of superconducting qubits, further improvements in their coherence and extensibility are still desirable and have become the key frontier of quantum computation research [9, 10, 11]. One direction of improvement relies on integrating the existing superconducting qubit modality and circuit quantum electrodynamics (cQED) architecture with advanced materials such as two-dimensional van der Waals (2D vdW) materials.

Since the first isolation of monolayer graphene in 2004 [12], 2D vdW materials have become a major field of interest in condensed matter physics, because they offer new platforms to explore novel physics and enable the engineering of different types of ultrathin devices. 2D vdW materials consist of individual atomic layers held together by weak out-of-plane van der Waals forces. Owing to the development of dry transfer techniques, different vdW materials can be stacked together with epitaxially precise and clean interfaces to create a wide variety of “vdW heterostructures” [13, 14]. As a result, 2D vdW materials provide us the potential to fabricate small-form-factor superconducting quantum devices with fewer defects and higher coherence than existing architectures. In fact, some necessary building blocks to construct superconducting qubits, such as parallel-plate shunt capacitors, and Josephson junctions, have already started to use vdW materials and have led to promising performance [15, 16, 17, 18, 19].

This thesis aims to contribute to the effort of incorporating the advantages of vdW materials into the circuit quantum electrodynamics (cQED) platform. In particular, our major goal is to characterize a vdW material system of interest - magic-angle twisted bilayer graphene (MATBG) - in the gigahertz-frequency regime. MATBG is a vdW heterostructure consisting of two monolayer graphene sheets stacked together with a twist angle of approximately 1.1 degrees between them. MATBG has recently emerged as a novel, highly tunable platform exhibiting a wide range of phases such as metal, insulating, and superconducting phases [5, 20]. While MATBG has been extensively studied via DC transport [2, 4, 21] and tunneling spectroscopy techniques [22, 23], to the best of our knowledge, no experimental attempt to investigate MATBG in the microwave regime has been yet demonstrated. There are two reasons that make microwave characterization of MATBG a crucial experiment:

- From a condensed-matter physics perspective, a fundamental but unresolved question about MATBG is its superconducting pairing mechanism. In unconventional superconductors, a possible probe to gain insight on that microscopic mechanism is a superfluid density measurement. In 3D, the superfluid density can be easily extracted by measuring the penetration depth of a static magnetic field into the superconductor [24, 25, 26]. In 2D materials such as MATBG, however, this method fails, as the penetration depth is no longer a simple function of superfluid density [27, 28]. A more promising method is to measure the superfluid density via their gigahertz-frequency AC conductance or related microwave characterization techniques.

- From a quantum engineer's perspective, MATBG's tunability and potentially high kinetic inductance are desirable to create voltage-tunable transmons [29] or high-impedance "protected" qubits such as fluxonium or zero-pi qubits [30, 31]. However, despite the well-developed cQED architectures and fabrication techniques for MATBG, incorporating them together in one device is nontrivial, with many technical complexities in noise filtering, delicate fabrication, superconducting contacts, to name a few. Characterizing the microwave properties of MATBG in a hybrid DC-microwave circuit would provide a path towards realizing MATBG-based superconducting qubits in the near future.

1.2 Thesis organization

This thesis begins with an introduction to magic-angle twisted bilayer graphene (MATBG) in chapter 2. Structural and electronic transport properties of MATBG, as well as how kinetic inductance can be used as a probe of superfluid density in MATBG, are discussed in detail. Chapter 3 is an overview of circuit quantum electrodynamics (cQED). Basic elements in cQED circuits used for microwave characterization and their physics are presented. In chapter 4, I describe the experimental approach, including DC-microwave hybrid circuit design and simulation, fabrication procedures, and the measurement setup employed to characterize the devices. Chapter 5 presents the experimental results from our first measurement round with five different twisted bilayer graphene devices. We successfully characterize the intrinsic transport response of one twisted bilayer graphene with DC characterization. With microwave characterization, we demonstrate how the resonator readout circuit is utilized to extract the inductance contribution of the twisted bilayer graphene device. Finally, in chapter 6, I conclude the thesis with a brief summary of our findings, their implications and emphasize the importance of future investigations.

Chapter 2

Overview of Magic-angle Twisted Bilayer Graphene

2.1 Geometry of graphene-based Moiré superlattices

The honeycomb lattice (lattice parameter $a = 2.46$ Å) of monolayer graphene has two sub-lattices, A and B. Basis vectors of A atoms are:

$$\mathbf{a_1} = \frac{a}{2}(3, \sqrt{3}), \tag{2.1}$$

$$\mathbf{a_2} = \frac{a}{2}(3, -\sqrt{3}), \tag{2.2}$$

and B atoms are shifted by $\delta = (\mathbf{a_1} + \mathbf{a_2})/3$.

In its natural form, the two layers of bilayer graphene are assembled in a vertical stack, where the B atoms of layer 2 lie above the A atoms of layer 1. This structure is called Bernal or AB-stacked bilayer graphene. In twisted bilayer graphene, we can view the system as the rotation of layer 2 by an angle θ about one common A_1B_2 position. This gives the emergence of a twisted moiré pattern.

Under some certain twist angles, the stacking A_1B_2 will reappear at a finite distance. The moiré system in such a case is called a 'commensurate' structure. We can define $\mathbf{T_1}$ and $\mathbf{T_2}$ as the primitive basis vectors of the commensurate structure. The

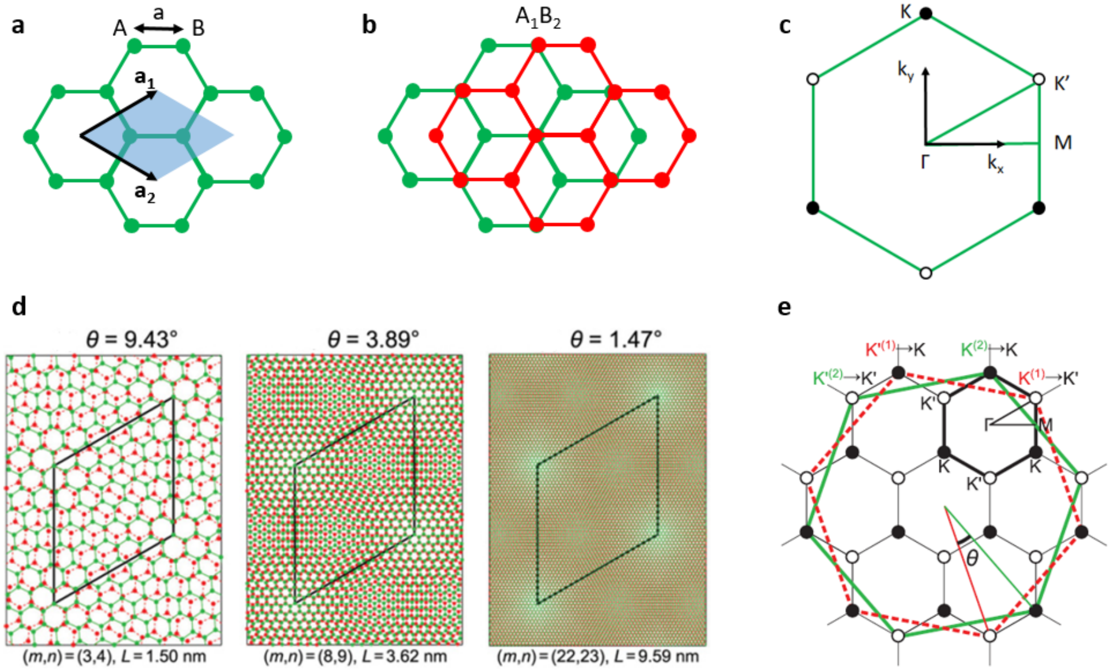

Figure 2-1: **a)** The honeycomb lattice of monolayer graphene with inequivalent A and B sublattices. **b)** The Bernal or AB-stacked bilayer graphene. In this natural assemble of bilayer graphene, B atoms of layer 2 lie above the A atoms of layer 1. **c)** The first Brillouin zone of monolayer graphene with two Dirac points K and K' labeled. **d)** The superlattice unit cell of twisted bilayer graphene with different commensurate twist angles. The smaller the twist angle is, the more atoms a superlattice unit cell contains. **e)** The formation of mini Brillouin zone in twisted bilayer graphene's reciprocal lattice. Two large hexagons in green and red represent the original first Brillouin zones of layers 1 and 2. Their Dirac points $K^{(1)}$, $K'^{(1)}$, $K^{(2)}$, and $K'^{(2)}$ are folded into two Dirac points of K and K' of mini Brillouin zone (the small black hexagon). Adapted from [1].

‘commensurate’ condition is:

$$\mathbf{T_1} = m\mathbf{a_1^{(1)}} + n\mathbf{a_2^{(1)}} = m'\mathbf{a_1^{(2)}} + n'\mathbf{a_2^{(2)}}. \tag{2.3}$$

Here, we can make the indices (m', n') equal to (n, m). A mathematic proof of commensuration indicates that the primitive basis vector $\mathbf{T_1}$ corresponds to m and $r = n - m$ being co-prime, and the twist angle θ is related to (m, r) by:

$$cos\theta = \frac{3m^2 + 3mr + r^2/2}{3m^2 + 3mr + r^2}. \tag{2.4}$$

One important parameter of commensurate structures is r. r can be intuitively understood as the number of Moiré periods to recover a ‘commensuration periodicity’. The simplest structures with $r = 1$ are called ‘minimal’ structures, or Moiré superlattices. The superlattice constant and the area of twisted bilayer graphene unit cell are given by:

$$L = a\frac{r}{2sin(\theta/2)} = a\frac{1}{2sin(\theta/2)}, \tag{2.5}$$

$$A = (\sqrt{3}/2)L^2. \tag{2.6}$$

In the reciprocal lattice of the Moiré superlattice, the mini Brillouin zone (MBZ) is generated from the difference between the two K (or K') momentum vectors of the two layers (Fig 2-1).

2.2 Band structure

2.2.1 Continuum model and tight binding calculation

Monolayer graphene is a semimetal with a gapless linear dispersion relation, resulting in the emergence of 2D massless Dirac fermions. In the presence of a second layer, a Bernal or AB stacked bilayer graphene has a gapless quadratic dispersion near the Fermi level. However, the electronic band structure of twisted bilayer graphene is much more complicated, because one superlattice unit cell contains a large number of atoms, especially at small twist angles. In addition, as discussed before, the commensurate structure is formed only at a discrete set of twist angles; for generic twist angles, we cannot use plane waves as the energy eigenstates. Therefore, calculating precisely the dependence of electronic band structures on twist angle is not a trivial task. The Hamiltonian of the system consists of three terms: two intra-layer terms describing hopping within each graphene sheet and one tunneling term describing hopping between layers.

First, we adopt the Dirac equation, which describes electron states close to the Dirac points of single-layer graphene, to describe the intra-layer terms of twisted bilayer graphene. In momentum space, those Hamiltonians are:

$$H_1 = \hbar v_0 \sigma \mathbf{k}^{(\mathbf{1})}, \tag{2.7}$$

$$H_2 = \hbar v_0 \sigma^{\theta} \mathbf{k}^{(\mathbf{2})}, \tag{2.8}$$

where v_0 is the Dirac velocity in monolayer graphene, $\mathbf{k}^{(\mathbf{1},\mathbf{2})}$ are momentum vectors measured from the corresponding layer's Dirac point, $\sigma = (\sigma^x, \sigma^y)$, $\sigma^{\theta} = e^{i\theta\sigma^z/2}\sigma e^{-i\theta\sigma^z/2}$, and $\sigma^{x,y,z}$ are Pauli matrices.

For convenience, we choose the center Γ of the mini Brillouin zone as the origin of momentum space. $\mathbf{k}$ indicates a momentum measured relative to Γ. $\mathbf{Q_1}$ and $\mathbf{Q_2}$ are reciprocal basis vectors in the mini Brillouin zone. $\Delta\mathbf{K} = \mathbf{K}^{(\mathbf{2})} - \mathbf{K}^{(\mathbf{1})}$ is the relative displacement of Dirac points between the two layers. Thus, $\mathbf{k}^{(\mathbf{1})}$ and $\mathbf{k}^{(\mathbf{2})}$ can be rewritten as:

$$\mathbf{k}^{(\mathbf{1})} = \mathbf{k} - \mathbf{Q_1} - \Delta\mathbf{K}, \tag{2.9}$$

$$\mathbf{k}^{(\mathbf{2})} = \mathbf{k} - \mathbf{Q_2} + \Delta\mathbf{K}. \tag{2.10}$$

H_1 and H_2 now only depend on $\mathbf{k}$, as $\mathbf{Q_{1,2}}$ and $\boldsymbol{\Delta}\mathbf{K}$ are fixed by the lattice geometry.

For interlayer tunneling, we need to find the Hamiltonian describing all processes in which an electron with momentum $\mathbf{q}^{(\mathbf{2})}$ of sublattice B of layer 2 hops to a momentum state $\mathbf{q^{(1)}}$ of sublattice A in layer 1. In twisted bilayer graphene, the hopping amplitude depends on the spatial separation between 2 sites of two layers.

We assume the hopping amplitude is a smooth function $t(\mathbf{r})$, which has the Fourier transform $\tilde{t}(\mathbf{\Delta q})$ in reciprocal space, with $\mathbf{\Delta q} = \mathbf{q^{(2)}} - \mathbf{q^{(1)}}$. The detailed calculation of hopping amplitudes shows that all amplitudes $\tilde{t}(\mathbf{\Delta q})$ are suppressed, except for three values: $\mathbf{\Delta q_0} = \mathbf{0}$, $\mathbf{\Delta q_1} = -\mathbf{Q_1}$, and $\mathbf{\Delta q_2} = \mathbf{Q_2}$ [1, 3]. In other words, when $\mathbf{k}$ is close to the Dirac cone of one layer, the three momentum values that it couples to lie at the same distance ΔK from the corresponding Dirac point of the other layer. Now, we have:

$$\tilde{t}_0(\mathbf{\Delta q_0}) = w \begin{pmatrix} 1 & 1 \\ 1 & 1 \end{pmatrix}, \tag{2.11}$$

$$\tilde{t}_1(\mathbf{\Delta q_1}) = w \begin{pmatrix} e^{-i2\pi/3} & 1 \\ e^{i2\pi/3} & e^{-i2\pi/3} \end{pmatrix}, \tag{2.12}$$

$$\tilde{t}_2(\mathbf{\Delta q_2}) = w \begin{pmatrix} e^{i2\pi/3} & 1 \\ e^{-i2\pi/3} & e^{i2\pi/3} \end{pmatrix}, \tag{2.13}$$

where w is the interlayer hopping energy, which can be determined from the experimentally known electronic bands of AB-stacked bilayer graphene ($w \approx 110$ meV).

To calculate the band structure, we truncate H_1, H_2, and $\tilde{t}(\mathbf{\Delta q})$ for the wave vectors $\mathbf{q^{(1,2)}}$ into a Hamiltonian matrix. Because the interlayer tunneling term is much smaller than the full bandwidth of monolayer graphene, the truncation mainly affects the low-energy part of the band structure near the original Dirac points. This leads to another important approximation of the continuum model: it is sufficient to restrict $\mathbf{q^{(1,2)}}$ to be close to the Dirac points (in the first mini Brillouin zone). Therefore, the interlayer Hamiltonian couples the state of wave vector $\mathbf{q^{(1)}} = \mathbf{k}$ of layer 1 to $\mathbf{q^{(2)}} \in \{\mathbf{k},\ \mathbf{k} - \mathbf{Q_1},\ \mathbf{k} + \mathbf{Q_2}\}$ of layer 2 and vice versa, the state of wave vector $\mathbf{q^{(2)}} = \mathbf{k}$ of layer 2 to $\mathbf{q^{(1)}} \in \{\mathbf{k},\ \mathbf{k} + \mathbf{Q_1},\ \mathbf{k} - \mathbf{Q_2}\}$ of layer 1. The Hamiltonian matrix is now simply a 12x12 matrix (6 wave vector points in reciprocal space, each having 2 components in the wave function),

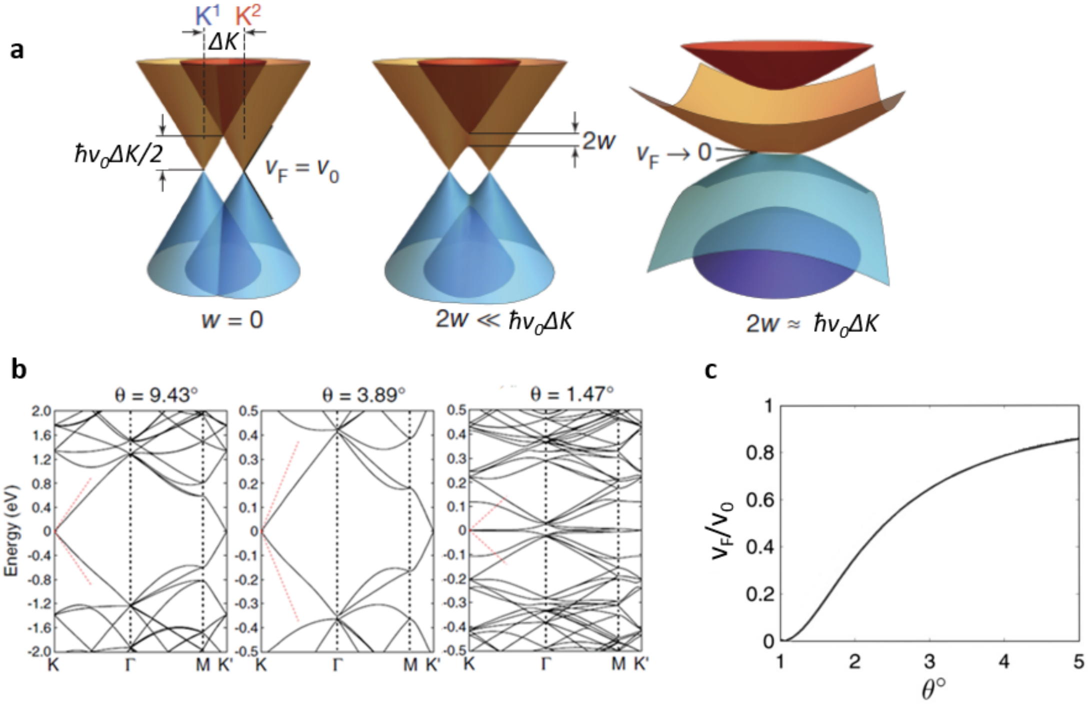

Figure 2-2: **a)** The effect of interlayer hybridization on the band structure of twisted bilayer graphene near valley points of the mini Brillouin zone [2]. The interlayer hopping energy w opens an energy gap near the energy of $\pm\hbar v_0 \Delta K/2$. The lowest band is flattened when the twist angle decreases and w becomes comparable to $\hbar v_0 \Delta K/2$ **b)** Band structure of twisted bilayer graphene for three different twist angles [1]. **c** The Fermi velocity is suppressed when the angle decreases and reaches 0 near 1.1^o. Adapted from [3].

$$H = \begin{pmatrix} H_{1\to1} & H_{2\to1} \\ H_{1\to2} & H_{2\to2} \end{pmatrix}, \tag{2.14}$$

$$H_{1\to1} = \begin{pmatrix} H_1(\mathbf{k}) & 0 & 0 \\ 0 & H_1(\mathbf{k}+\mathbf{Q_1}) & 0 \\ 0 & 0 & H_1(\mathbf{k}-\mathbf{Q_2}) \end{pmatrix}, \tag{2.15}$$

$$H_{2\to2} = \begin{pmatrix} H_2(\mathbf{k}) & 0 & 0 \\ 0 & H_2(\mathbf{k}-\mathbf{Q_1}) & 0 \\ 0 & 0 & H_2(\mathbf{k}+\mathbf{Q_2}) \end{pmatrix}, \tag{2.16}$$

$$H_{2\to1} = H_{1\to2}^{\dagger} = \begin{pmatrix} \tilde{t}_0 & \tilde{t}_1 & \tilde{t}_2 \\ \tilde{t}_1 & 0 & 0 \\ \tilde{t}_2 & 0 & 0 \end{pmatrix}. \tag{2.17}$$

The low energy band structure $\epsilon(\mathbf{k})$ is calculated by the diagonalization of the Hamiltonian matrix in Eq 2.14.

2.2.2 Formation of flat bands

We can summarize the tight binding calculation result as follows:

- For large twist angle, the low-energy dispersion relation is linear, similar to that of single-layer graphene, but with a slightly different Fermi velocity.

- When the twist angle is reduced, the band at the Dirac point flattens (Fermi velocity decreases).

- At the so-called "magic angle", the Fermi velocity vanishes, corresponding to a manifestly flat band [32]. By using the most simple model discussed in 2.2.1, the Fermi velocity is given by:

$$v_F(\theta) = v_0 \frac{1-3\alpha^2}{1+6\alpha^2}, \tag{2.18}$$

where $\alpha = w/(\hbar v_0 \Delta K)$ and $\Delta K = 4\pi\theta/3a$. Using this formula, the first magic angle, at which $v_F = 0$, is $\theta_{magic} \approx 1.1^o$.

2.3 Transport properties

2.3.1 Superlattice-induced insulating states

The superlattice-induced insulating state is attributed to the gaps opened at the central point of the mini Brillouin zone. Intuitively, the gap is opened because of the hybridization between two Dirac cones at $\mathbf{K^{(1)}}$ and $\mathbf{K^{(2)}}$. The energy where the gap occurs is approximately $\pm\hbar v_0 \Delta K/2$. As a result, when the twist angle decreases, the energy where these gaps occur becomes smaller.

For large angles θ, these gaps are generally inaccessible in transport experiments, because they occur at high energy. For smaller angles θ, Cao et al. have reported the observations of insulating states at $\theta = 1.8^o$, where the thermal activation gap is about 50 meV [33]. The total carrier density is $n \approx \pm 7.5 \times 10^{12}$ cm^{-2}, which implies that a filled low-energy band requires 4 electrons per superlattice unit cell (each Dirac cone $\mathbf{K^{(1,2)}}$ contributes two 1/2-spin electrons),

$$n = \frac{4}{A} = \frac{4}{(\sqrt{3}/2L^2)}. \tag{2.19}$$

2.3.2 Correlated insulating states at half-filling

When θ is near the magic-angle value, experiments have shown that, besides the superlattice-induced insulating state, there is another pair of novel insulating states occurring at half-filling density. These states are not observed at a temperature higher than approximately 4 K, which means there is a metal-insulator transition occurring at this temperature. The thermal activation gap of these states is about 0.3 meV, which is two orders of magnitude smaller than the superlattice-induced insulating gap [2].

This behavior is not expected in single-body systems. At the magic angle, the

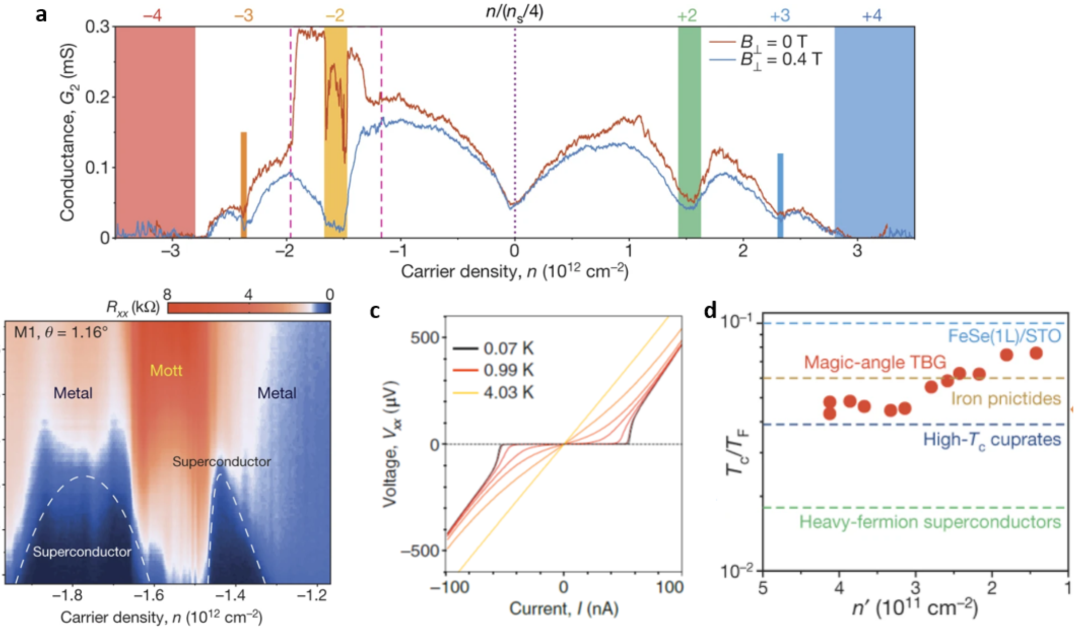

Figure 2-3: Evidence of unconventional superconductivity in MATBG [4, 3, 5] includes **a)** The sharp enhancement of 2-probe conductance near half-filling at zero field is suppressed in 0.4 T perpendicular B field. **b)** The phase diagram of superconducting domes. **c)** Non-linear I-V curves showing a temperature-tunable critical current. **d)** The variation of ratio between superconducting critical temperature and Fermi temperature as a function of carrier density. The ratio in MATBG is above the trend line of most cuprate, heavy-fermion, organic superconductors, suggesting the superconductivity may not originate from weak electron-phonon coupling.

band is flat, and the bandwidth $W = \max_{\mathbf{k},\mathbf{k}' \in MBZ}[\epsilon(\mathbf{k} - \epsilon(\mathbf{k}')]$ is strongly suppressed. Meanwhile, the Coulomb interaction between 2 electrons can be estimated as $U = e^2/(4\pi\epsilon_0 d)$, where d is the effective dimension of each site (same length scale as the moiré period). Near the magic angle, W is small, and the ratio U/W can be larger than 1. Therefore, qualitatively, a plausible explanation for these insulating states is the Coulomb interaction between electrons (Mott-like insulating states).

2.3.3 Unconventional superconductivity

When MATBG is doped by electrostatic gating slightly away from the correlated insulating state of the lower flat band, an unconventional superconducting state is observed. The highest critical temperature achieved experimentally is approximately 3 K [5]. Moreover, the ratio between superconducting critical temperature and Fermi temperature T_c/T_F in MATBG is approximately 0.05, whereas T_c/T_F in conventional superconductors is on the order of 10^{-5}. High T_c/T_F ratio in MATBG suggests that the superconductivity in MATBG may not originate from weak electron-phonon coupling. Noticeably, compared to other known two-dimensional superconducting materials, the carrier density at the superconducting state of MATBG is much lower, 1.2×10^{12} cm^{-2}, compared to 1.5×10^{13} cm^{-2} in $LaAlO_3/SrTiO_3$ interfaces and 7×10^{13} cm^{-2} in doped MoS_2, marking the high tunability of MATBG superconductivity with low gate voltage. [4, 21].

The discovery of superconductivity in MATBG has sparked significant interest both theoretically and experimentally about its superconducting pairing mechanism. Some models predict that superconducting and "Mott-like" insulating states are intimately connected, which suggests an unconventional, purely electronic pairing mechanism [34, 35, 36]. On the other hand, other models predict a more conventional phonon-mediated pairing mechanism, which may be enhanced by a high density of states and strong electron correlation [37, 38]. However, a direct measurement of the pairing symmetry in MATBG remains an unresolved question in the field.

2.4 Kinetic inductance and superconductivity of MATBG

One promising experimental approach that may allow us to gain insight into the microscopic mechanism of superconductivity in MATBG is microwave electrodynamics. A direct probe of the superconductor's intrinsic response in the microwave regime is the kinetic inductance, which accounts for energy stored in the supercurrent as the kinetic energy of the Cooper pairs.

The kinetic inductance in a superconductor is related to the superfluid density of Cooper pairs in a simple model that equates the inductive energy with the total kinetic energy of Cooper pairs [24]. In a superconductor of length 1m, width 1m, thickness d, and Cooper pair density n_s, then the square kinetic inductance is calculated as follows:

$$E_{kin} = L_{kin}^{\square} I^2, \tag{2.20}$$

$$L_{kin}^{\square} = \frac{d n_s 2 m_e v^2}{(n_s 2 e v d)^2} = \frac{m_e}{2 n_s e^2 d}. \tag{2.21}$$

The kinetic inductance per square can be further expressed in terms of the bulk magnetic penetration depth $\lambda^2 = \frac{m_e}{2\mu_0 n_s e^2}$. Then, we find $L_{kin}^{\square} = \mu_0 \frac{\lambda^2}{d} = \mu_0 \lambda_{\perp}$, where $\lambda_{\perp}$ is the effective penetration depth of the superconducting film.

Using the weak-coupling Bardeen–Cooper–Schrieffer (BCS) theory, one can also derive a relation between the kinetic inductance and the superconducting gap. To do that, we need first to introduce the so-called "two-fluid" model by Mattis-Bardeen, in which the AC electrodynamics is described by combining the response of "superconducting" and "normal" electron fluids to alternating electromagnetic fields. In this model, the superconductor is equivalent to a circuit of a resistor and an inductor in series. If we assume that the geometric inductance is negligible compared to the kinetic inductance, the impedance per square is given by $Z^{\square} = R^{\square} + i\omega L_{kin}^{\square}$. On the other hand, following Glover and Tinkham [27, 28], the conductivity of the superconducting state can be written in a complex form $\sigma = \sigma_1 - i\sigma_2$. In the limit where ω is much smaller than $\omega_g = \Delta/\hbar$, where Δ is the superconducting gap, then $\sigma_1 \ll \sigma_2$, where σ_2 relates to the normal state conductivity σ_n as follows:

$$\frac{\sigma_2}{\sigma_n} = \frac{\pi\Delta}{\hbar\omega}\tanh\frac{\Delta}{2kT}. \tag{2.22}$$

Using the limit $\sigma_1 \ll \sigma_2$, we can derive $L_{kin}^{\square} = 1/(\omega\sigma_2 d)$ while the normal resistance per square $R_n^{\square} = 1/(\sigma_n d)$. Therefore, the relation between kinetic inductance, superconducting gap, and normal resistance is:

$$L_{kin}^{\square} = \frac{\hbar R_n^{\square}}{\pi\Delta}\frac{1}{\tanh\frac{\Delta}{2kT}}. \tag{2.23}$$

In short, the kinetic inductance of a weak-coupling BCS superconductor is directly related to its Cooper pair density, penetration length, superconducting gap, and normal resistance. Any substantial deviation from this model would suggest an anomalous superconducting state. Thus, we expect the kinetic inductance to be a useful probe for unconventional superconductivity in MATBG.

Although it is likely that kinetic inductance of MATBG would deviate from the value for a conventional BCS superconductor, for the purpose of circuit design (to be explained in Chapter 4), we still use BCS theory to estimate the MATBG kinetic inductance. Using experimental results of critical temperature $T_c \approx 1$ K and normal resistance $R_n^{\square} \approx 2$ k$\Omega/\square$ [4], we have:

$$\Delta_{BCS}(T = 0\text{K}) = 1.76 k_B T_c \approx 0.15 \text{ meV}, \tag{2.24}$$

$$L_{kin}^{\square}(T = 0\text{K}) = \frac{\hbar R_n^{\square}}{\pi\Delta} \approx 2.76 \text{ nH}/\square. \tag{2.25}$$

This estimated inductance is much larger than geometric inductance of a square thin film, which is on the order of 10^{-6} nH/$\square$ [39]. Thus, the result is consistent with our earlier assumption that the kinetic inductance is the main inductance contribution. Noticeably, this estimated value of MATBG kinetic inductance is one order of magnitude larger than for granular Aluminum [40], which suggests that MATBG can be a promising material for inductively shunted superconducting circuits (such as fluxonium qubits). Again, this observation emphasizes that the impact of MATBG microwave characterization is not only to investigate the microscopic mechanisms of its superconductivity, but also to explore the potential for using this material system in superconducting qubits.

Chapter 3

Overview of Circuit Quantum Electrodynamics

3.1 Scattering parameters in microwave network analysis

The concepts of scattering parameters or S-parameters in microwave networks describe how electromagnetic energy "power wave" propagates per unit time through a multi-port linear system. For the purpose of this thesis, we only consider a two-port network where the reference impedance of all ports is $Z_0 = 50\ \Omega$. The incident and reflected power waves for each port are defined as:

$$a_i = \frac{1}{2}\frac{V_i + Z_0 I_i}{\sqrt{\mathrm{Re}\{Z_0\}}}, \tag{3.1}$$

$$b_i = \frac{1}{2}\frac{V_i - Z_0^* I_i}{\sqrt{\mathrm{Re}\{Z_0\}}}, \tag{3.2}$$

where V_i, I_i are the voltage and current flowing into the i-th port. Then, we can write the S-parameters in matrix form $\mathbf{S}$ to relate vectors of incident and reflected power waves, $\mathbf{a}$ and $\mathbf{b}$ [41]:

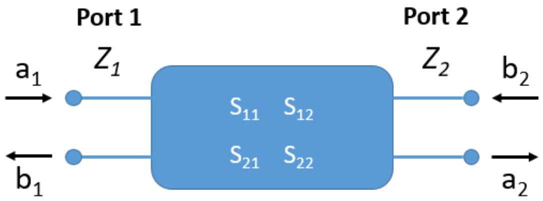

Figure 3-1: S-matrix of a two-port network

$$\mathbf{b} = \mathbf{S}\mathbf{a}, \tag{3.3}$$

$$\mathbf{a} = \begin{pmatrix} a_1 \\ a_2 \end{pmatrix}, \mathbf{b} = \begin{pmatrix} b_1 \\ b_2 \end{pmatrix}, \tag{3.4}$$

$$\mathbf{S} = \begin{pmatrix} S_{11} & S_{12} \\ S_{21} & S_{22} \end{pmatrix}, \tag{3.5}$$

In the experiment using a vector network analyzer (VNA), one can easily measure both amplitude and phase of the matrix elements S_{mn}, which indicates how much signal is transmitted (or reflected) from port n to port m. How the impedance of the system between ports varies as a function of frequency is extracted via S-parameter measurements.

3.2 Physics of superconducting microwave resonators

3.2.1 Transmission lines

The first element investigated here is the coplanar waveguide (CPW) transmission line. A CPW consists of a conductor strip of width s, on top of a dielectric medium ϵ, horizontally separated by a distance w from a pair of ground planes. The characteristic impedance $Z_0 = \sqrt{L/C}$, where L and C are distributed inductance and capacitance of CPW, is given by:

$$Z_0 = \frac{30}{\sqrt{(1+\epsilon)/2}} \frac{K(k_0')}{K(k_0)}, \tag{3.6}$$

$$k_0 = \frac{s}{s+2w}, \tag{3.7}$$

$$k_0' = \sqrt{1-k_0^2}, \tag{3.8}$$

where $K(k_0)$ is the complete elliptic integral with modulus k_0 [8].

3.2.2 Half and quarter-wave resonators

A distributed resonator is a resonant circuit formed from a section of transmission line, where the resonant frequency corresponds to the existence of a standing wave along the resonator's length. The two types of resonators we will discuss here have one open end (not connected to the ground), with the other end being either open or shorted to the ground. For simplicity, we first discuss the case of a lossless resonator (no resistance). Similar to the standing wave on a string, due to the abrupt change of impedance at the resonator's ends, there exists a voltage node at the grounded end and a voltage antinode at the open end of the resonator. Therefore, for a resonator with two open ends, the resonance occurs when the resonator's length l is an integer number of half-signal-wavelength, $l = n\lambda/2$, $n = 1, 2, 3...$, and is called a "half-wave resonator". For a resonator with one open end and one shorted end, the resonance occurs when $l = n\lambda/4$, $n = 1, 3, 5...$, and is called a "quarter-wave resonator" [6].

For its fundamental mode, the position dependence of voltage and current for a half-wave resonator of length l is:

$$V(x) = V_m \cos(\pi x/l), \tag{3.9}$$

$$I(x) = I_m \sin(\pi x/l); \tag{3.10}$$

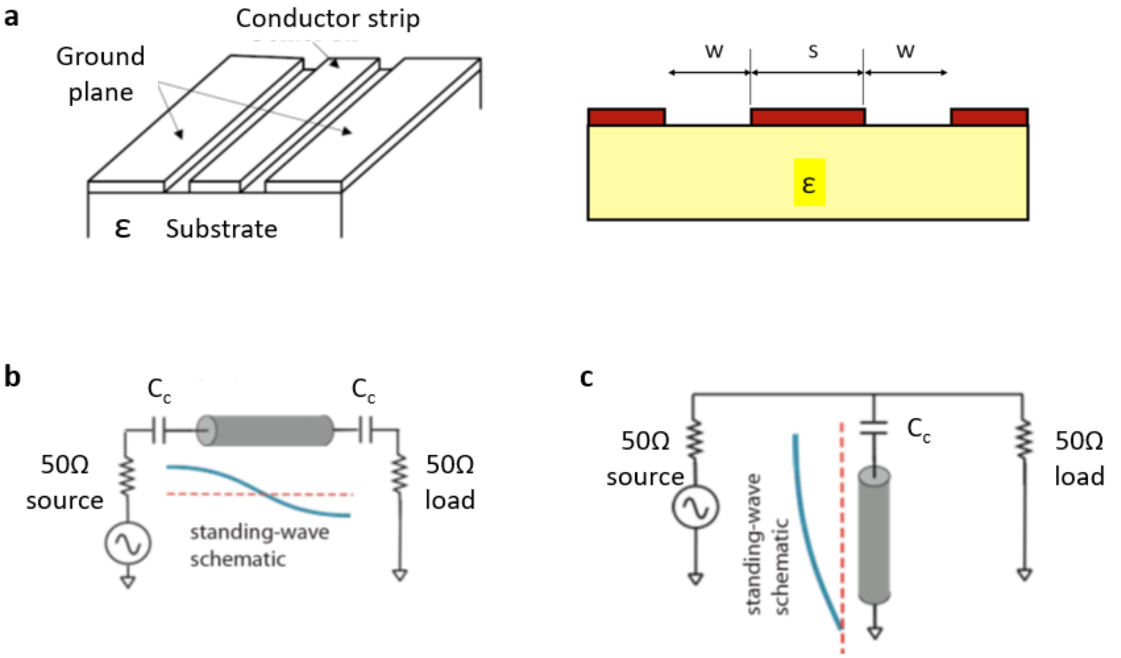

Figure 3-2: **a)** The coplanar waveguide geometry. The width of conductor strip is s and the gap between conductor strip and the ground plane is w. **b)** Configuration of a half-wave resonator. **c)** Configuration of a quarter-wave resonator. Adapt from [6].

and for a quarter-wave resonator is:

$$V(x) = V_m \cos(\pi x/2l), \tag{3.11}$$

$$I(x) = I_m \sin(\pi x/2l). \tag{3.12}$$

Any change in the local inductance of the resonator (e.g. additional kinetic inductance) will cause a greater response at a location with higher current. Therefore, the shorted end of a quarter-wave resonator, which is the point of maximal current, is one of the most ideal locations to incorporate a MATBG device to measure its kinetic inductance. Thus, we now need to discuss in depth the physics of general CPW quarter-wave resonators. By applying elementary circuit theory to a differential-length lumped-element model of a distributed resonator, one can derive the wave equation for voltage phasor:

$$\frac{\partial^2}{\partial x^2}\tilde{V}(x) - \gamma^2 \tilde{V}(x) = 0, \tag{3.13}$$

where γ is the propagation constant of the resonator and is related to its distributed inductance L_r, resistance R_r and capacitance C_r through the expression $\gamma = \alpha + i\beta = \sqrt{(R_r + i\omega L_r)(i\omega C_r)}$. Parameters α and β are respectively called the attenuation constant and the phase constant of the resonator. The input impedance of a quarter-wave resonator of length l is obtained by solving the wave equation with boundary conditions [7, 8]:

$$Z_{in} = Z_{0r} \tanh \gamma l = Z_{0r} \frac{1 - i \tanh \alpha l \cot \beta l}{\tanh \alpha l - i \cot \beta l}, \tag{3.14}$$

where $Z_{0r} = \sqrt{L_r/C_r}$ is the characteristic impedance of the resonator.

The attenuation constant α vanishes for the lossless case, and the fundamental resonance corresponds to $\beta_0 l = \pi/2$, $\omega_0 = \pi/(2l\sqrt{L_r C_r})$, and a divergent Z_{in} (finite voltage and zero current at the open end).

For the small loss case, where $\alpha l \ll 1$, and at a frequency $\omega = \omega_0 + \Delta\omega$ close to the resonance frequency, Eq 3.14 reduces to:

$$Z_{in} = \frac{Z_{0r}}{\alpha l + i\pi\Delta\omega/2\omega_0}. \tag{3.15}$$

We notice that this impedance has the same form as a parallel RLC circuit's impedance near its resonance frequency:

$$Z_{in} = \frac{1}{1/R' + 2i\Delta\omega C'} \tag{3.16}$$

Therefore, a quarter-wave resonator has an equivalent circuit comprising of 3 lumped elements, with R', L', C' in parallel, with $R' = \frac{2}{l}\frac{L_r}{R_r C_r}, C' = \frac{l}{2}C_r, L' = \frac{8l}{\pi^2}L_r$.

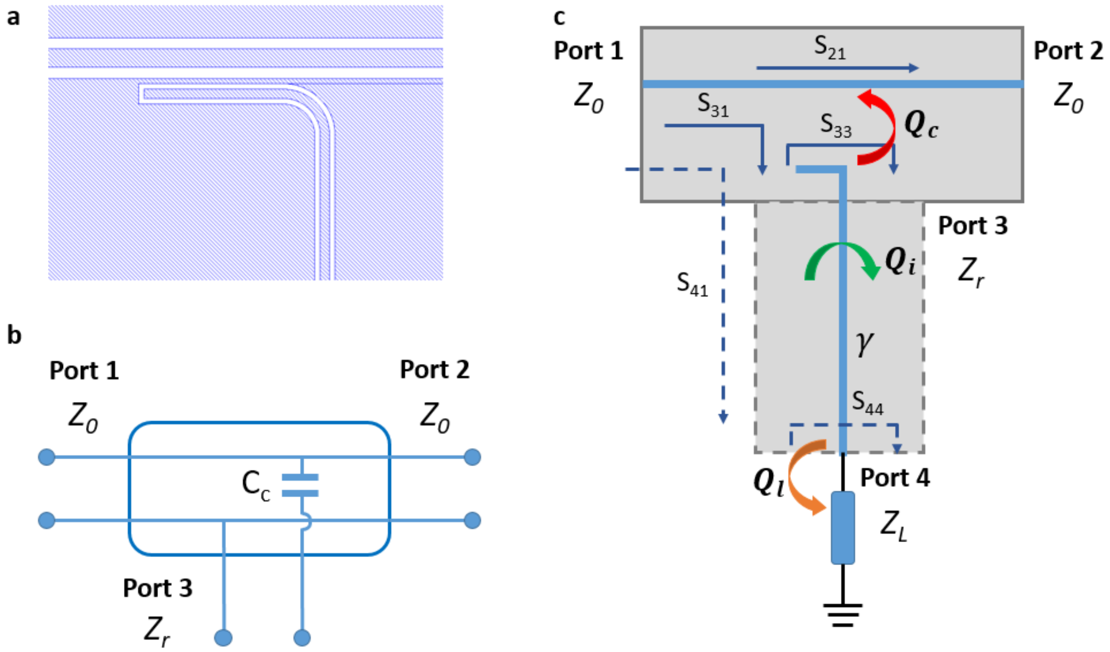

Figure 3-3: **a)** The resonator is capacitively coupled to a transmission line via a "elbow" coupler. **b)** The equivalent three-port network. **c)** The signal flow diagram of the three-port network. Three loss channels - internal, coupling, load dissipation - are characterized by three quality factors Q_i, Q_c, Q_l as denoted in the diagram. Adapted from [7].

3.2.3 Resonator capacitively coupled to a transmission line

We consider a resonator read-out circuit consisting of a transmission line (lossless impedance Z_0), an "elbow" coupler, and a quarter-wave resonator (impedance Z_r and propagation constant γ). The coupler capacitively couples the resonator and the transmission line used to probe the resonator; thus, its equivalent circuit element is a coupled capacitor C_c. We analyze this read-out circuit using the network analysis approach introduced by Gao [7].

First, we consider a 3-port network: port 1 and 2 with reference impedance Z_0, and port 3 with reference impedance Z_r. We denote $\delta_0 = \omega C_c Z_0$ and $\delta_r = \omega C_c Z_r$. Considering the weak coupling regime, where $\delta_r, \delta_0 \ll 1$, the scattering matrix is given by:

$$S = \begin{pmatrix} -i\delta_0/2 & 1 & i\sqrt{\delta_0\delta_r} \\ 1 & -i\delta_0/2 & i\sqrt{\delta_0\delta_r} \\ i\sqrt{\delta_0\delta_r} & i\sqrt{\delta_0\delta_r} & \sqrt{1-2\delta_r\delta_0} \end{pmatrix}. \tag{3.17}$$

We have used the following approximations:

- The direct transmission through the transmission line is close to unity ($S_{21} \approx 1$).
- Because the dimension of the coupler is small compared to the wavelength, the 3-port network is considered to be reciprocal ($S_{31} = S_{13}$, $S_{32} = S_{23}$).
- Port 1 and 2 are symmetric ($S_{13} = S_{23}$).
- The 3-port network is lossless and the phase change at the open end of resonator is negligible ($S_{33} \approx \sqrt{1-2|S_{31}|^2}$).

Extending the 3-port network to include the quarter-wave resonator with port 4 at the shorted end of the resonator, we have the following modified scattering matrix elements:

$$S_{41} = S_{14} = S_{42} = S_{24} = S_{31}e^{-\gamma l} \tag{3.18}$$

$$S_{44} = S_{33}e^{-2\gamma l} \tag{3.19}$$

Now, via a straightforward signal-flow analysis, we write the total transmission from port 1 to port 2 as:

$$\tau_{21} = S_{21} + \frac{S_{41}S_{24}}{1-\Gamma S_{44}} = 1 + \frac{|S_{31}|^2}{e^{2\gamma l} + S_{33}}, \tag{3.20}$$

where Γ is the reflection coefficient at port 4. In this case, the shorted end of the resonator corresponds to $\Gamma = -1$.

3.2.4 Quality factors of the resonator

There are two main loss channels of the energy stored in a quarter-wave resonator:

- The internal loss due to finite distributed resistance of the resonator,
- The coupling loss due to leaked energy from the resonator to port 1 and port 2 via the coupling capacitor.

The rates of these energy losses are quantified correspondingly by an internal quality factor Q_i and a coupling quality factor Q_c [8, 42].

The internal quality factor is determined via the propagation constant:

$$\gamma = \alpha + i\beta = i\beta(1 - \frac{i}{2Q_i}) = \sqrt{(R_r + i\omega L_r)(i\omega C_r)}. \tag{3.21}$$

Using a straightforward algebraic calculation, we derive $Q_i = \omega L_r / R_r$.

In one cycle of a traveling wave inside the quarter-wave resonator, it is reflected twice at port 3. In each reflection, it leaks an energy fraction $|S_{31}|^2$ and $|S_{32}|^2$ respectively to port 1 and port 2. Therefore, the coupling quality factor is:

$$Q_c = \frac{2\pi}{2(|S_{31}|^2 + |S_{32}|^2)} = \frac{\pi}{2|S_{31}|^2}, \tag{3.22}$$

$$|S_{31}|^2 = \frac{\pi}{2Q_c}, \tag{3.23}$$

$$S_{33} = \sqrt{1 - 2|S_{31}|^2} \approx 1 - \frac{\pi}{2Q_c}. \tag{3.24}$$

At a frequency f close to the fundamental mode resonance frequency $f_0 = 1/(4l\sqrt{L_r C_r})$, we have:

$$e^{2\gamma l} \approx -1 - \frac{\pi}{2Q_i} - i\pi\frac{f - f_0}{f_0}. \tag{3.25}$$

Plugging in all of these approximations (Eqs 3.22 - 3.25), the total transmission

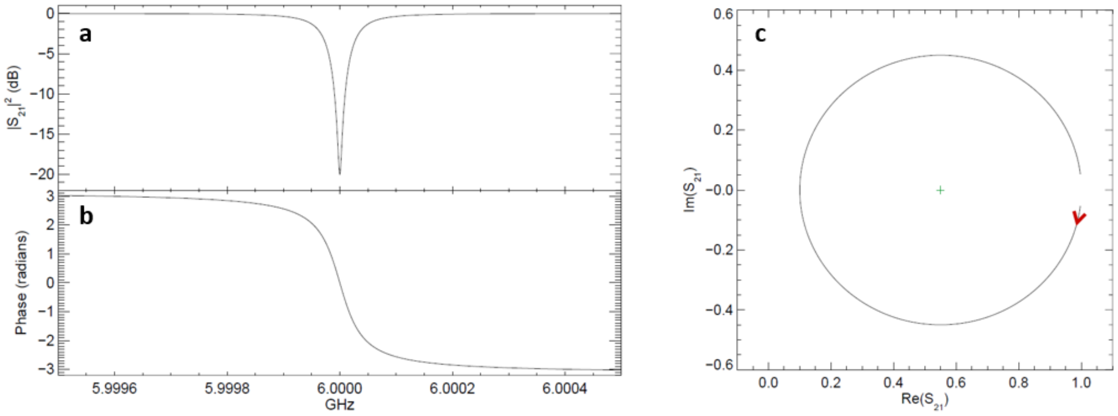

Figure 3-4: Transmission signal past a quarter-wave resonator near its resonance frequency. The resonator has $f_0 = 6$ GHz and $Q_c = 10^5$. At resonance frequency, **a)** the transmission amplitude has a dip. **b)** The transmission phase has a steep change. **c)** The trajectory of transmission signal in the complex plane is a circle. The red arrow shows the direction of increasing frequency. Adapted from [8].

is:

$$\begin{aligned} \tau_{21} &\approx 1 - \frac{\frac{\pi}{2Q_c}}{\frac{\pi}{2Q_i} + \frac{\pi}{2Q_c} + i\pi\frac{f-f_0}{f_0}} \\ &\approx 1 - \frac{\frac{Q_r}{Q_c}}{1 + 2iQ_r\frac{f-f_0}{f_0}}. \end{aligned} \tag{3.26}$$

Here, Q_r is the total quality factor of the resonator, $1/Q_r = 1/Q_c + 1/Q_i$.

We can easily see from the above formula that near the resonance frequency $f = f_0$, the transmission features a dip and a sharp phase change. The trajectory of τ_{21} in the complex plane is a circle with diameter Q_r/Q_c (Fig 3-4).

3.2.5 Hybrid resonator with impedance at closed end

Now we consider the case where one end of the quarter-wave resonator is connected to the ground via a lumped loading element with a small but non-negligible impedance

Z_l. The reflection coefficient at port 4 changes to:

$$\Gamma = \frac{Z_l - Z_r}{Z_l + Z_r} \approx 1 - 2r_l - 2ix_l, \tag{3.27}$$

$$\frac{Z_l}{Z_r} = r_l + ix_l. \tag{3.28}$$

We can define another quality factor associated with the dissipation via the load impedance $Q_l = \pi/(4r_l)$. Repeating the same process as the case of zero load impedance, we obtain a similar form of transmission fraction:

$$\tau_{21} \approx 1 - \frac{\frac{Q'_r}{Q_c}}{1 + 2iQ'_r\frac{f-f'_0}{f'_0}}, \tag{3.29}$$

but with new total quality factor and shifted resonant frequency:

$$\frac{1}{Q'_r} = \frac{1}{Q_i} + \frac{1}{Q_c} + \frac{1}{Q_l}, \tag{3.30}$$

$$f'_0 = f_0(1 - \frac{2x_l}{\pi}). \tag{3.31}$$

From this analysis, one can measure the changes in resonant frequency and total quality factor to determine the load impedance connected to the end of a quarter-wave resonator.

Chapter 4

Experimental Approach

As we discussed in chapter 3, a resonator readout circuit can be used to extract the impedance of a load connected to the closed end of the quarter-wave resonator. In our case, a gate-tunable MATBG device is connected to the closed end of a quarter-wave resonator. Thus, measuring the dependence of the resonant frequency with respect to the applied gate voltage of the MATBG allows us to probe microwave responses of MATBG for its different voltage-gating-dependent matter phases. This is the central idea of our experimental approach to measuring the kinetic inductance of MATBG. In this chapter, we describe in detail how a resonator readout circuit is designed, incorporated to MATBG device, and measured in the gigahertz-frequency regime.

4.1 Circuit design and simulation

4.1.1 Resonator readout circuit

Transmission line

The standard characteristic impedance of microwave cables in RF measurements is 50Ω. To maximize the power transfer between cables and the transmission line and avoid frequency-dependent transmission, we have to match their characteristic impedance. In other words, we need to design the dimensions of the CPW transmission line to yield the characteristic impedance of 50Ω. Using equation 3.6 for the

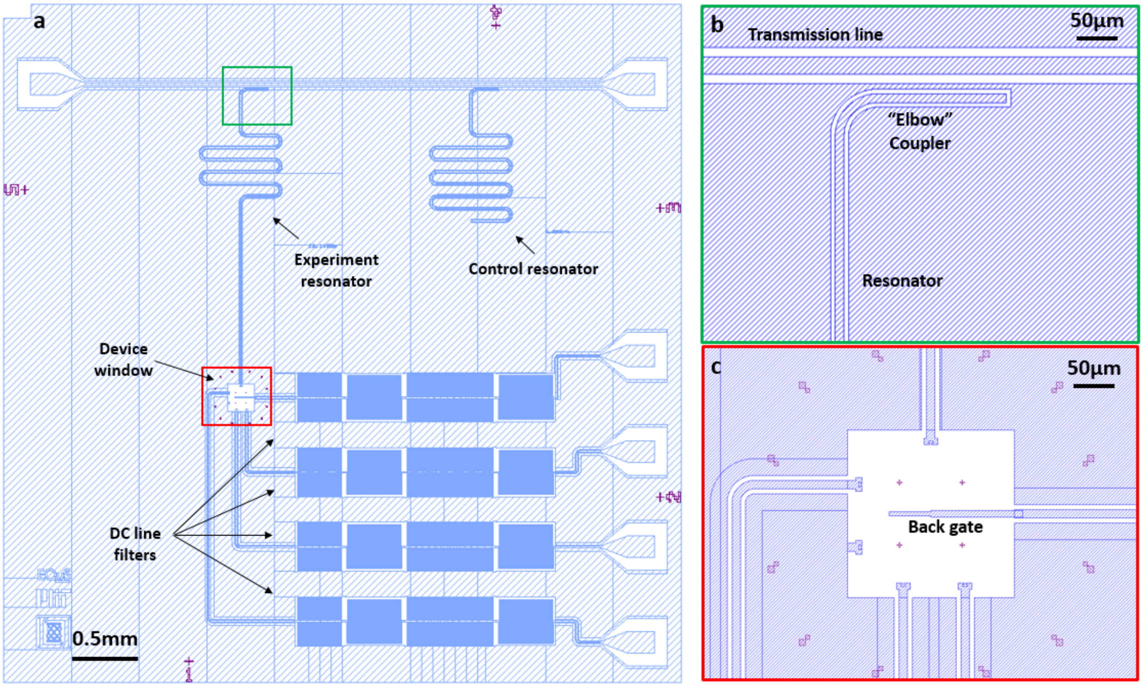

Figure 4-1: **a)** The CAD layout design of a 5 mm × 5 mm microwave circuit chip. White regions represent the Silicon substrate and blue regions represent the Aluminum metal layer. **b)** Green box shows how a resonator is capacitively coupled to the transmission line via an "elbow" coupler. **c)** Red box is the zoomed-in design of a 200 μm ×200 μm device window with DC backgate.

Silicon (Si) substrate $\epsilon = 11.45$, the ratio of w/s of CPW has to be 5/3. In our design, we choose $s = 20$ μm and $w = 12$ μm. The transmission line's length is 3.8 mm to exploit almost the full length of our standard 5 mm × 5 mm qubit chip and allows for multiple resonators to be coupled to it on the same chip. At the two ends of the transmission line, we design two bonding pads to later connect the transmission line to a package interposer and on to microwave cables.

Control resonator

We design a standard quarter-wave resonator capacitively coupled to the transmission line. This control resonator (without MATBG) is used as a reference to extract the coupling strength and the propagation constant in the experiment resonator. To save space on the chip, we use the resonator with an "elbow" coupler and a meandering structure. We choose the total length of this resonator to be 4853 μm. Similar to

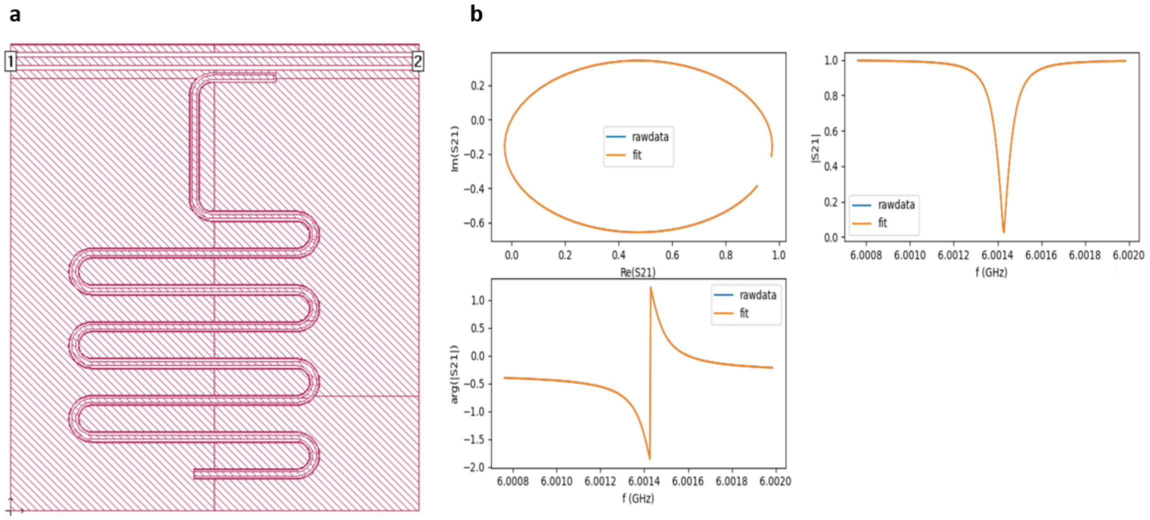

Figure 4-2: **a)** The control resonator design is imported into SONNET software. Two ports 1 and 2 are placed at two ends of the cropped transmission line. **b)** Fitting results of the simulation data using Eq 3.26.

the transmission line, the resonator also has the coplanar waveguide geometry where $s_r = 10$ μm and $w_r = 6$ μm to create a characteristic impedance of $Z_0 = 50$ Ω. To determine the resonance frequency and quality factors, we use an RF simulator called SONNET to obtain the frequency dependence of the S-parameters and fit the simulation data to the transmission formula presented in chapter 2. Fig 4-2 is the setup and results of a SONNET simulation on our control resonator.

To extract the resonance frequency and quality factors from the dependence of the S-parameter on the signal frequency, we use the fitting method introduced by Probst et.al. [43]. The fitting parameters resulting from the simulation above are $f_0 = 6.0014$ GHz and $Q_{r0} = 52{,}561$. This resonance frequency f_0 is purposefully chosen, because our measurement setup works best in the frequency range of $3 - 12$ GHz We can calculate the distributed inductance and capacitance of the control resonator via resonance frequency and quality factors using the results in section 3.2.4:

$$C_r = \frac{1}{4lf_0Z_0} \approx 1.7168 \times 10^{-10} \text{ F/m}, \tag{4.1}$$

$$L_r = {Z_0}^2 C_r \approx 4.2919 \times 10^{-7} \text{ H/m}. \tag{4.2}$$

Experiment resonator

The structure of our experiment resonator is similar to the control resonator, except that the hanging end is now located in a window where we will integrate a gate-tunable MATBG device that will connect the resonator to the ground plane. There are certain constraints in designing this experiment resonator:

- The central frequency of the experiment resonator (quarter-wave frequency) should be far enough from that of the control resonator that they don't overlap. Ideally, we need the separation to be larger than the width of resonance peaks in the resonators to enable the detection of both peaks. For the control resonator described above, that width is $\Delta f \approx f_0/Q_0 = 0.114$ MHz, where $f_0 = 6.0014$ GHz is the resonance frequency and $Q_0 = 52561$ is the total quality factor of the control resonator.

- The resonant frequencies of the experiment resonator corresponding to different matter phases exhibited by MATBG should ideally remain within the frequency range of the measurement setup.

We choose the total length of the experiment resonator to be 4958 μm. A SONNET simulation shows that the experiment resonator has a resonance frequency of $f_r = 5.3534$ GHz when its end is grounded (i.e. MATBG is a shorted circuit with no inductance). Thus, the separation between resonance frequencies of two resonators is sufficient to satisfy the first constraint.

The resonant frequency of the experiment resonator terminated with MATBG is difficult to simulate precisely, due to a wide range of complicated phases in MATBG. However, we can estimate the bounds of these resonant frequencies with simulations. The upper and lower bounds of frequency correspond to when the termination is open (half-wave resonator), or when it is an ideal inductor carrying the kinetic inductance of the MATBG estimated in the previous chapter (quarter-wave resonator with load). The SONNET simulation results show that these frequencies are 3.6070 GHz and 12.134 GHz respectively. This range is within the ideal frequency range of the measurement setup and satisfies the second constraint.

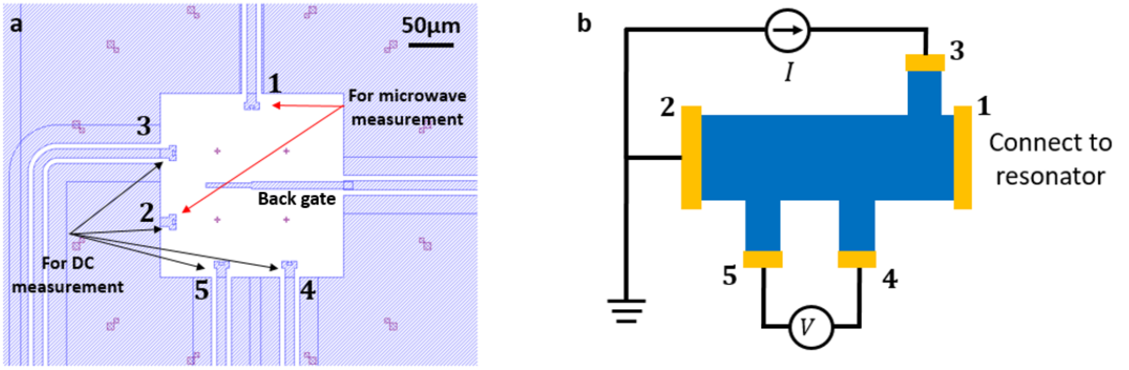

Figure 4-3: **a)** The device window design. Three DC lines 3,4,5 and ground connector 2 make up 4 DC probes. The resonator's connector 1 and ground connector 2 are used for microwave measurement. **b)** The 4-probe DC measurement configuration using 2,3,4,5 connectors.

Device window, DC probes, and filters

The device window is where the MATBG device is transferred, and it is attached at the hanging end of the experiment resonator. This window is a 200 nm × 200 nm square. The DC gate used to tune charge carrier density in MATBG is designed in the middle of this window. The gate has two regions with different widths (5 μm and 8 μm)

As mentioned earlier, our goal is to characterize the microwave response of the resonator to different matter phases in MATBG. To achieve this goal, we need to first map out different phases in MATBG as a function of the applied gate voltage. This is normally done with quasi-DC transport measurements. Therefore, the circuit design also incorporates a 4-probe measurement capability. In our design, three DC lines connect to the device window with bonding pads, and together with the ground plane connector, make up the 4 DC probes (Fig 4-3).

In this hybrid circuit, the quality factor of the microwave circuit is sensitive to photon loss due to the coupling of the MATBG device with its DC contacts and DC backgate. Thus, to maintain a high quality factor, we introduce to each DC line an on-chip band stop filter. The purpose of this band stop filter is to prevent the signal within our frequency range of interest $3 - 12$ GHz from dissipating via the DC line. In our design, we use a standard LCLC filter with meandering inductors

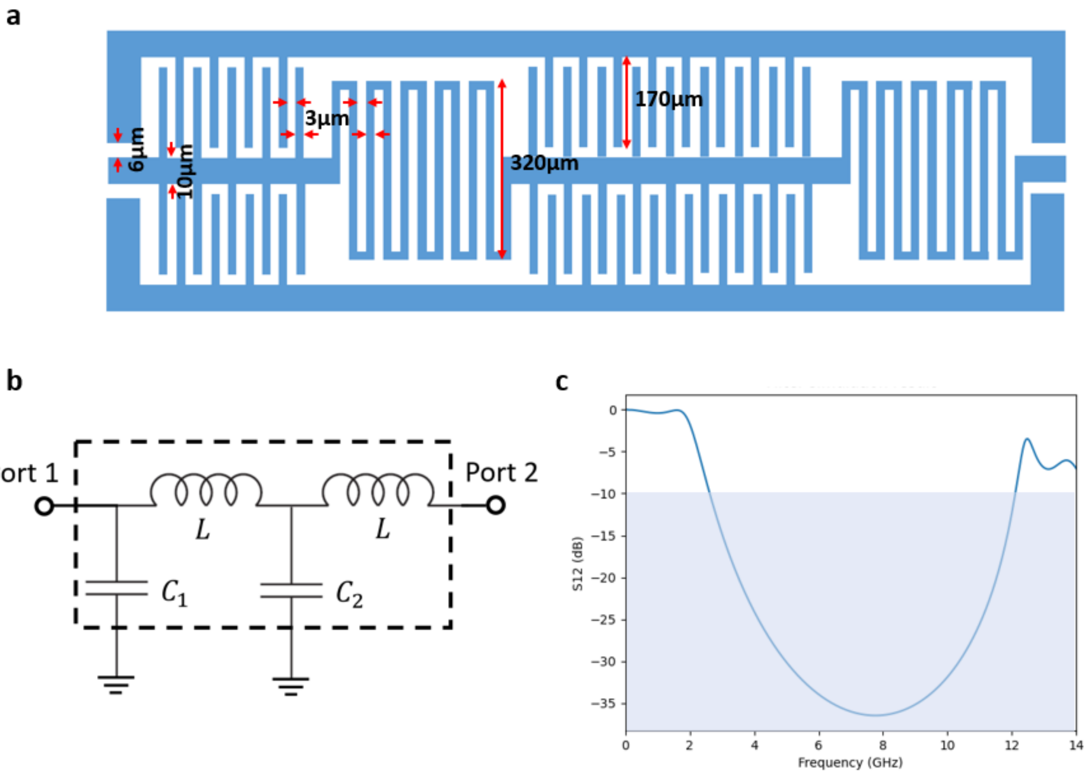

Figure 4-4: **a)** Demonstration (not drawn in precise scale) of the LCLC filter design with meandering inductors and interdigitated capacitors. The size and length of each element in the filter are labelled. b) Equivalent lump-element circuit of the filter. **c)** The SONNET simulation result of the filter. This filter provides an attenuation greater than 10dB for the frequency range $3-12$ GHz.

and interdigitated capacitors to minimize their footprint. The size and length of each element in the filter are carefully chosen so that the stop band matches the frequency range of interest. Fig 4-4 is the SONNET simulation result of the designed band stop filter. We can see that the frequency range $3-12$ GHz corresponds to an attenuation greater than 10dB.

4.2 Device fabrication

This section describes the process of fabricating on-chip microwave circuits, twisted bilayer graphene devices, and integrating the devices onto corresponding circuits. Although each of the above fabrication processes has been separately well-established, the procedures to combine them together are not trivial and involve several detailed modifications, which are emphasized below.

4.2.1 Microwave circuit fabrication

Special thanks to David Kim and our collaborators at MIT Lincoln Laboratory for helping us fabricate the on-chip microwave circuits.

Based on the finalized design, we first need to prepare the on-chip microwave circuits, which eventually are the substrates on to which we transfer the twisted bilayer graphene stacks. We first deposit a 250 nm-thick aluminum film onto a 2-inch Si wafer by molecular-beam epitaxy (MBE) evaporation. The transmission line, coplanar waveguide resonators, DC filters, and device windows are defined using photolithography and standard Al wet-etching. Then, 100 nm-thick platinum alignment markers and 50 nm-thick aluminum bottom gates are subsequently deposited onto the chip using e-beam lithography and e-beam metal evaporation. The bridge between deposited bottom gates and their corresponding filters are made via in-situ ion milling and Aluminum deposition. The purpose of this step is to remove the surface Al oxide, minimize contact resistance, and thereby maintain high quality factor. Finally, the wafer is diced into 5 mm × 5 mm pieces onto which the twisted bilayer graphene stacks can be deposited. Fig 4-5 is the optical image of a complete microwave circuit chip after fabrication. We also check the roughness and thickness of the fabricated backgate via AFM. AFM results indicate that the thickness result is 48 ± 3 nm. The backgate's surface does not have polymer residue from the fabrication process. However, there is excessive aluminum, with thickness less than 20 nm, accumulated on two sides of the backgate. We attribute this to the imperfect anisotropy of the lithography and metal-deposition processes. Since the excessive aluminum is relatively sparse and thinner than the backgate, we expect that it would not affect the subsequent fabrication steps.

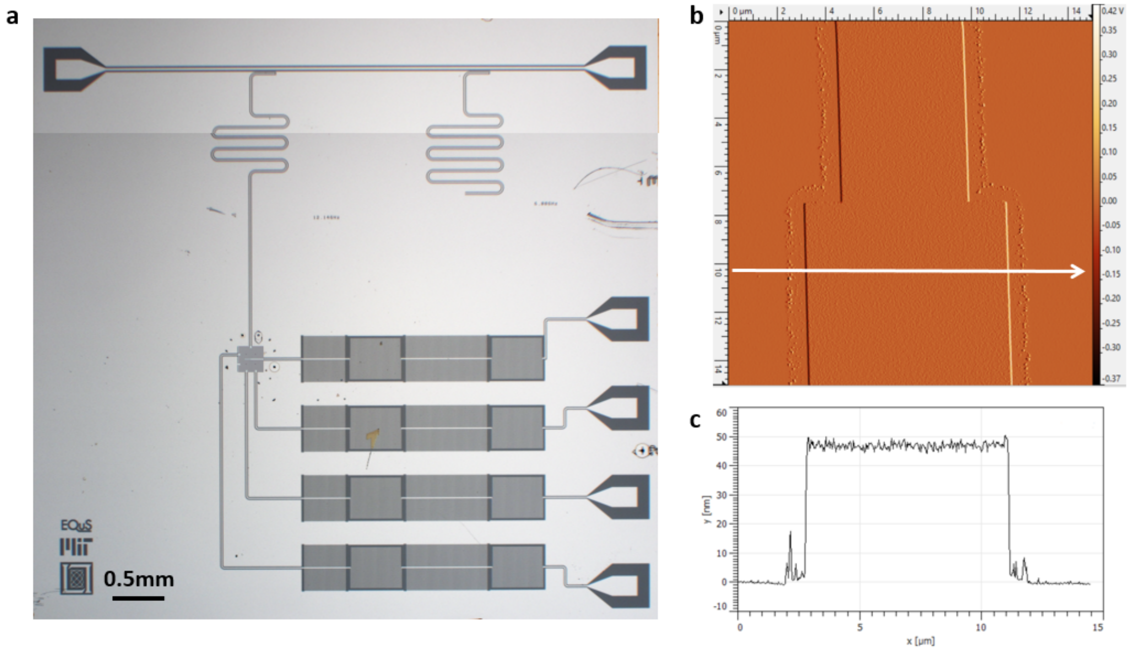

Figure 4-5: a) The complete microwave circuit chip after fabrication. **b)** AFM amplitude image of the backgate. **c)** Height profile of the white line cut in **b)**. The size and thickness of the backgate agrees well with the design parameters. The backgate's surface does not have polymer residue.

4.2.2 Twisted bilayer graphene stacking

A van der Waals heterostructure of MATBG consists of MATBG encapsulated between two hBN (hexagonal Boron Nitride) flakes. The encapsulation is particularly important to insulate MATBG from the bottom metal gate as well as to protect MATBG from defects, nanofabrication residues, and twist angle relaxation during the fabrication process. We use adhesive tape to mechanically exfoliate graphene and hBN flakes from their bulk crystals and deposit them onto clean Si/SiO$_2$ substrates. After adhering a small piece of crystal onto the tape, we copy it a few times to reach the desired density and thickness. Then we press the tape on top of the substrate and slowly peel the bulk crystal away. As a result, thin flakes are left on the Si/SiO$_2$ substrate. For graphene exfoliation, we heat the substrate to 220^{o}C before depositing graphene in order to reduce the tape residues and increase the yield of monolayer graphene flakes. For hBN exfoliation, we anneal the substrate with deposited hBN flakes at 350^{o}C for 3 hours with a constant flow of Argon and Hydrogen through the annealing tube to remove tape residues on top of hBN flakes. The flakes are selected by both bright-field and dark-field optical inspection. Typically, we choose wrinkle-free, crack-free large monolayer graphene, 60-70 nm - thick bottom hBN, and 30-50 nm - thick top hBN flakes.

Next, we assemble the flakes into a complete heterostructure using the dry pick-up and transfer technique. This technique utilizes a polymer "stamp", consisting of a 3 mm × 3 mm × 1 mm polydimethylsiloxane (PDMS) cushion and a polycarbonate (PC) film mounted on a glass slide. The stickiness of PC film increases with temperature; therefore, we use that sticky surface to pick up hBN flakes from the Si/SiO_2 substrate. When the temperature reaches the melting point, above 155^{o}C, the PC film melts, detachs from the PDMS cushion, and sticks to the substrate. The PC film can be dissolved by soaking the substrate in chloroform for 10 minutes.

The transfer setup used for heterostructure assembly consists of a sample stage to secure the substrate, and a precise micro-manipulator to hold the glass slide with the PDMS-PC stamp. This manipulator controls the horizontal movement for alignment purposes and the vertical movement for stamp engaging/disengaging purposes.

The detailed step-by-step recipe for assembling a twisted bilayer graphene stack is described as follows [33, 2, 44].

1. Pick up and deposit the bottom hBN flake onto the microwave circuit chip

    - Heat the substrate containing the bottom hBN flake to 90^{o}C and engage the stamp with the hBN flake, wait 1 minute for the stamp to conform well to the hBN flake.
    - Cool down the substrate slowly so that the stamp starts to contract on its own and picks up the hBN flake by adhesive force at around 60^{o}C.
    - Align and engage the hBN flake with the back gate on the microwave circuit chip at room temperature.
    - Heat the substrate to 160^{o}C, then slowly lift up the stamp. The melted PC will detach from the PDMS and stick to the substrate.

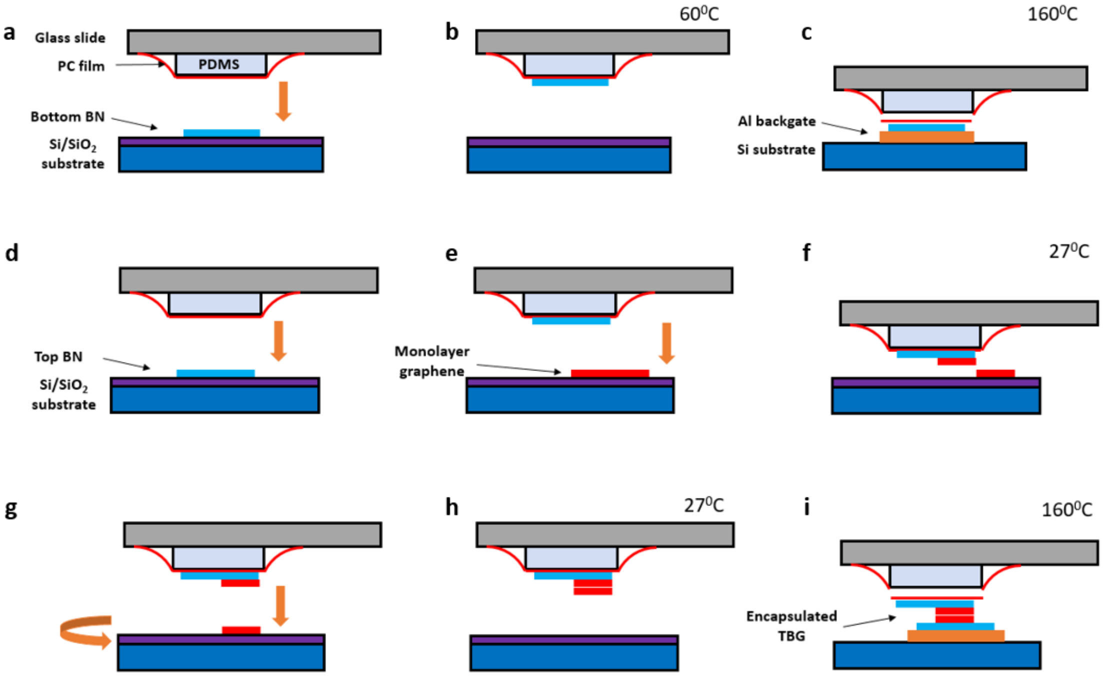

Figure 4-6: Twisted bilayer graphene fabrication steps. **a)** Mount the glass slide and Si/SiO$_2$ substrate containing bottom hBN flake into the transfer system. Heat the substrate to 90^{o}C and engage the stamp with the hBN flake. **b)** Cool down the substrate slowly to pick-up the hBN flake. **c)** Transfer the bottom hBN flake onto the backgate of the microwave circuit chip and break the PC film at 160^{o}C. **d)** Repeat **a** and **b** to pick-up top hBN flake. **e)** Align and engage top hBN flake with the monolayer graphene flake at room temperature. **f)** Pick up one half of monolayer graphene flake. **g)** Align and engage the top hBN + one half of graphene flake with the rotated remaining half. **h)** Pick up the remaining half of graphene flake at room temperature. **i)** Transfer the stack onto the bottom hBN flake and break the PC film at 160^{o}C.

    - After dissolving the PC film using chloroform, the bottom hBN surface is likely contaminated with PC residues. We then clean these residues with an AFM tip cleaning technique. An AFM tip is driven in contact mode back and forth on the hBN surface, and the soft residues are swept away by the tip.

2. Assemble magic-angle twisted bilayer graphene stack by "tear-and-stack" technique.

    - Pick up the top hBN (similar to picking up the bottom hBN).
    - Align and engage the top hBN flake with one half of the graphene flake and disengage slowly. The van der Waals force between hBN and graphene will pick up half of the graphene flake.
    - After disengaging completely from the substrate, rotate the substrate by $\sim 1.13 - 1.17$ degree, align and engage the hBN/graphene with the other half of graphene flake, then disengage slowly to pick it up.
    - Deposit top hBN/TBG stack on the bottom hBN (in a similar way as depositing bottom hBN on the back gate), dissolve the PC film, and we are left with a complete hBN/MATBG/hBN stack.

3. Since air bubbles normally accumulate between flakes during the transfer process, we need to perform an AFM inspection to identify a bubble-free, irregularity-free region and pattern our device accordingly in a later step.

4.2.3 Patterning and making contacts

We now need to pattern the stack into the desired shape and make contacts connecting the MATBG device to the resonator, filters, and the ground plane on the microwave circuit chip.

We utilize electron beam lithography (EBL) and plasma etching techniques to pattern our device. The chip is first covered with a polymer resist mask composed

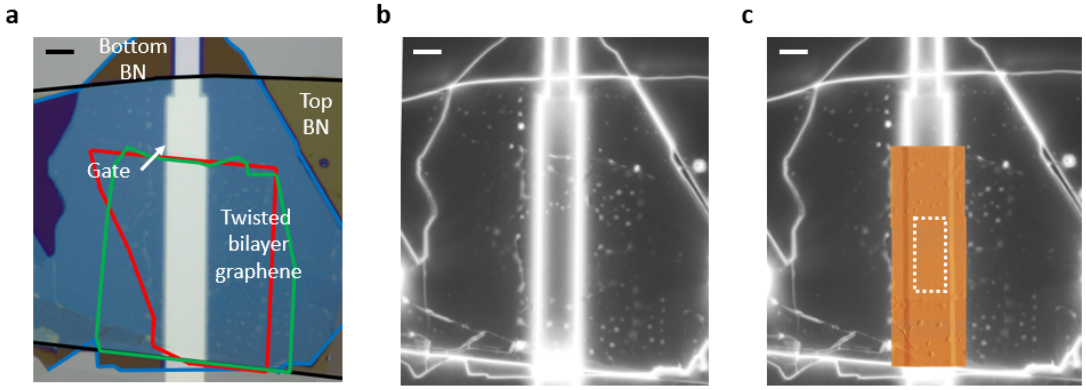

Figure 4-7: **a, b)** Optical images in bright-field and dark-field mode of a completed twisted bilayer graphene stack on top of the backgate. **c)** Align the AFM image to the dark field optical image to identify a bubble-free region (dash white rectangle) to pattern the device.

of polymethyl methacrylate (PMMA). We perform two rounds of spinning PMMA 950A5 at 4000 RPM for 60 seconds, anneal to dry the chip at 180^{o}C for 3 minutes between spins. We notice that our substrate easily accumulates charge, which impacts the imaging with the electron beam, leading to poor lithography; to avoid this from happening, we also spin on top of the PMMA resist a layer of anti-charging agent (Discharge H2O) at 1500 RPM for 20 seconds and 3500 RPM for 25 seconds. Next, we perform EBL with a dose of 2000 μC/cm^2 at 10 nA current, and cold development using a solution made with Isopropyl Alcohol:H_2O = 3:1 by weight at 0^{o}C for 60 seconds, resulting in the pattern in Fig. 4-8. hBN and graphene are then etched away by a plasma generated by O_2 and CHF_3 gases in a reactive ion etching (RIE) system. The resist is dissolved in Acetone for 10 minutes before the contacting step.

We again cover the chip with a PMMA resist mask and Discharge H2O. The difference is the resist used in this step consists of two layers: the bottom one is PMMA 495A5 and the top one is PMMA 950A2. This double-layer creates an undercut during the e-beam lithography and allows a better lift-off in the subsequent step. We then perform EBL again with a similar dose and a cold development. In order to make planar contacts with the MATBG device, the top hBN needs to be etched away. Therefore, we perform a highly selective RIE etching for 10-13 seconds with a plasma generated by Ar, O_2, and CHF_3. This etching recipe has an etch rate of 5 nm hBN

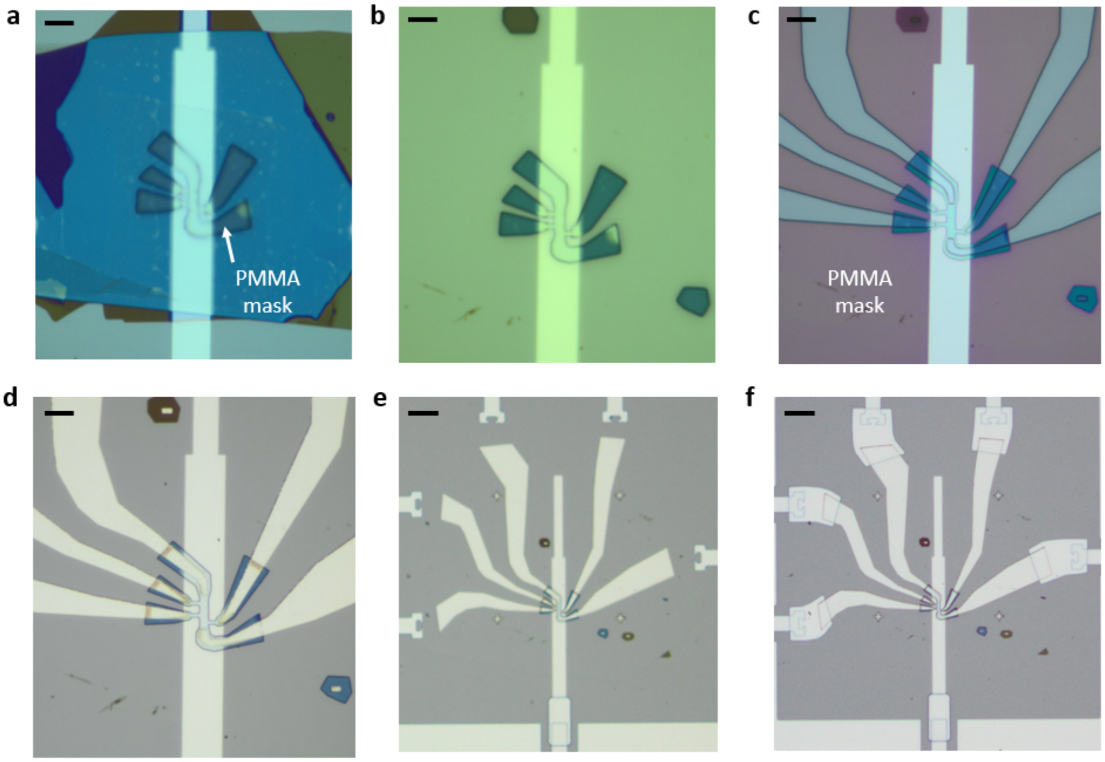

Figure 4-8: Optical images after each patterning and making contacts step. **a)** The PMMA mask is patterned with e-beam lithography to cover the device area. **b)** The material outside the mask is etched away. **c)** Another PMMA mask is patterned to open the contact regions. **d)** After etching the top hBN in the contact regions, Aluminum is deposited to form the contacts. **e)** Zoom-out image of the device with Aluminum contacts. **f)** A complete device after ion-milling and depositing Aluminum bridges to fully connect the contacts with the resonator, filters, and the ground plane.

(about 10 monolayers of hBN) per second and one monolayer of graphene per 20 seconds. We then deposit 7 nm of Titanium as the sticking layer and 70-80 nm of Aluminum to form the contacts via thermal evaporation at base pressure $1 - 3 \times 10^{-7}$ Torr. We remove the resist and residual metals in a lift-off process: submerging the chip in Acetone for 6-7 hours, then squirting Acetone on the chip with a syringe to peel away Aluminum film.

Finally, we perform an in-situ ion-milling and 250 nm-thick Aluminum bridge deposition step to fully connect the contacts with the resonator, filters, and the ground plane. The resist in this step consists of one bottom layer MMA (methyl methacrylate) EL9 and one top layer PMMA 950A5. After another lift-off, the device is

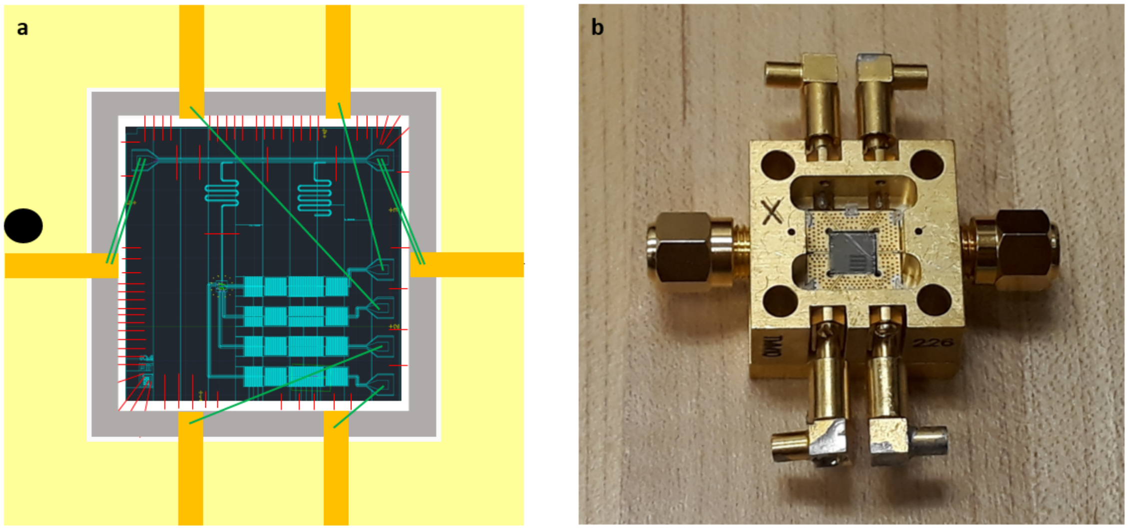

Figure 4-9: **a)** Wire-bonding diagram of the microwave circuit chip. Green lines indicate the wire bonds between bonding pads to SMA and SSMB connectors. Red lines indicate the wire bonds between ground planes around the transmission line and resonators and the ground plane of the package. **b)** Photo of a package containing a fully-wire-bonded chip.

complete.

4.3 Measurement setup

4.3.1 Packaging and wire-bonding the microwave circuit chip

Again, thanks to David Kim and our collaborators at MIT Lincoln Laboratory for helping us with packaging and wire-bonding.

The microwave circuit chip with a complete MATBG device is mounted inside a standard "small-qubit package" made of gold plated copper. In order to reduce possible unwanted package modes (spurious resonances), we only use a drilled-out pedestal with four tiny posts at the package's corners to support the chip.

Fig 4-9 shows the wire-bonding diagram of the microwave circuit chip. The transmission line is connected to two K (SMA-compatible) connectors. These connectors are used to apply and readout the microwave pulses through the transmission line. The DC backgate and three DC lines are connected to four SSMB connectors on two sides of the package. Lastly, the ground planes around the transmission line and resonators are wire-bonded together and to the ground plane of the package. We use a large number of bonds to make sure that the entire chip shares a single, homogeneous ground reference and to reduce inductance to package ground.

VdW 2D devices are sensitive to electrostatic discharge (ESD). Therefore, it is crucial to use ESD safe containers during transportation and to ground ourselves when we wire-bond or mount the devices/packages.

4.3.2 Dilution refrigerator

All measurements presented in this thesis are performed in a cryo-free dilution refrigerator (BlueFors XLD refrigerator). Fig 4-10 shows the photo of our dilution fridge with different temperature stages. This cryo-free system uses a closed-loop cryocooler to lower the temperature from room temperature down to 4 K. The lowest stage is the refrigerator mixing chamber, where the temperature can stably reach approximately 10 mK. The dilution cooling process in this stage uses a mixture of two Helium isotopes: ^{3}He and ^{4}He. The cooling mechanism exploits the heat absorption of ^{3}He from the environment when it undergoes the transition from a ^{3}He-concentrated phase to a diluted phase composed of 6.4% ^{3}He and 93.6% ^{4}He.

The device package is mounted in this mixing chamber stage. In order to protect the measurement from any noise caused by external magnetic fields, the package is shielded by two superconducting shields and one mu-metal shield.

4.3.3 Measurement Setup

DC line filtering

DC transport measurements of mesoscopic devices at base temperature (approximately 10 mK) is susceptible to electromagnetic noise, which is caused by "hot" electrons from higher temperature stages being injected into the device. These "hot" electrons are decoupled from phonons at base temperature, and thermalize more slowly than at warmer temperatures [45]. Therefore, filtering this electromagnetic

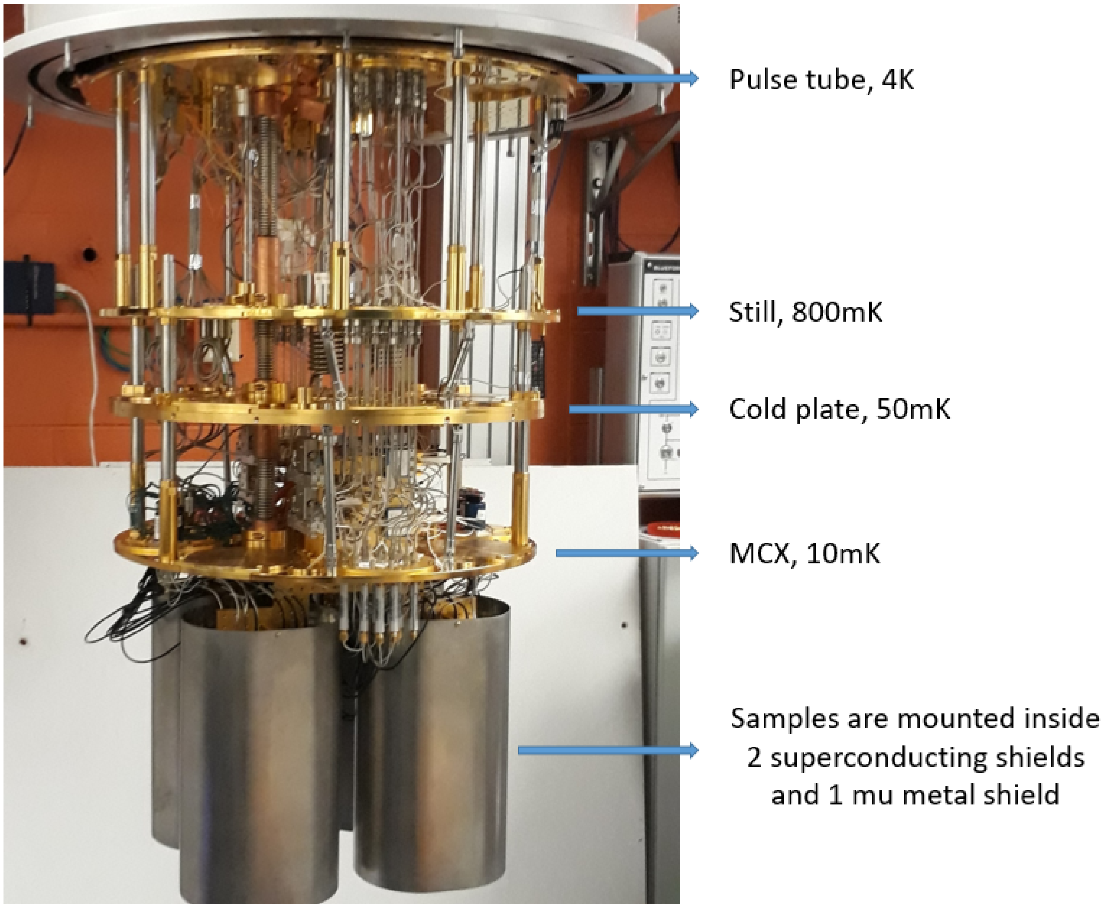

Figure 4-10: Photo of our BlueFors dilution refrigerator. Different lowest temperatures corresponding to different stages of the refrigerator are labelled.

noise is crucial to effectively thermalizing the experiment at milikelvin temperatures. Since the thermal energy of electrons at 4 K corresponds to electromagnetic noise at the GHz frequency range ($f = 4k_B/h \approx 83$ GHz), we use low-pass filters connected to DC lines to isolate our devices from high-frequency noise in transport measurements.

In our experiment, each DC loom, which contains 24 DC lines, is connected to a combination of two filters: an RC filter at 4 K stage and a copper powder filter at the mixing chamber stage. The RC filter consists of a 50 Ω resistor and two 30 nF capacitors, providing a cut-off frequency at 53kHz. The powder filter contains a copper tube filled with copper powder and a long resistive wire coil inside. It utilizes the skin effect damping and provides effective attenuation for the signal with frequencies above 300 MHz. A broad-band low-pass filter is achieved via the combination of these two filters. Furthermore, to avoid thermal noise caused by the filters themselves, both filters are thermally anchored to their corresponding host stages by having large metal surfaces in contact with the stages.

Transport characterization setup

The transport characterization uses a standard AC+DC differential measurement with a current bias. The electronic set up at room temperature outside the refrigerator consists of two DC voltage sources, one lock-in amplifier and one voltage amplifier (Fig 4-11). A gate voltage, provided by a Yokogawa GS200 DC source, is applied to the device's backgate via the DC line labeled "gate". A DC current bias signal, provided by QDevil QDAC DC source, and an AC current bias signal, provided by the output of SRS 860 lock-in amplifier, are combined and sourced to the device through the DC line labeled I. Two resistors with resistance much larger than the device resistance (which is on the order of kΩ) are used to create a current bias from voltage sources: $R_{\text{ac bias}} = 1$ MΩ and $R_{\text{dc bias}} = 2$ MΩ. The frequency of the AC current is set to 17 Hz, which is a frequency sweet spot to avoid interference from the power line frequency 60Hz. In order to measure the differential resistance of the device, the AC voltage response between two DC lines labeled $V+$ and $V-$ is amplified by a SRS 560 low-noise voltage amplifier (amplifying the signal by a factor of 1000), then measured

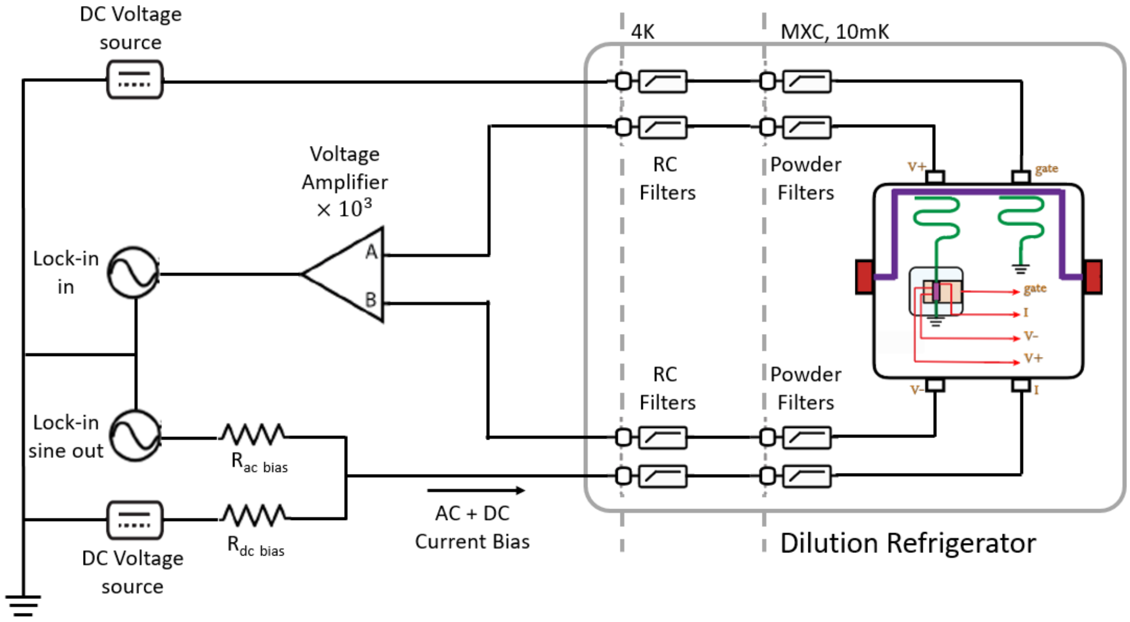

Figure 4-11: Diagram of the DC measurement setup. The DC line filters inside the dilution fridge and the electronic setup at room temperature outside the fridge are described in section 4.3.3.

by the lock-in input channel. All instruments mentioned above and the refrigerator share a common ground. Fig 4-11 is the diagram of our DC characterization setup.

In this setup, the low-frequency current bias provided by the lock-in is used to measure the differential resistance R_{xx} of the device. On the other hand, the role of the DC current bias is to overcome the effect of possible proximitized superconductivity [45, 46] due to aluminum-graphene contacts. Specifically, in order to measure the intrinsic transport response of graphene devices, this DC current bias needs to be larger than the critical current of proximitized superconductivity.

Microwave Characterization Setup

Fig 4-12 shows the microwave wiring diagram. Along each microwave line at different stages of the fridge, there are some combinations of circulators and isolators to guide the microwave signals while preventing noise from going back to the device, attenuators to filter out thermal noise, high-pass and low-pass filters to limit the frequency range of interest to 3 - 12 GHz, and amplifiers to amplify the output signal.

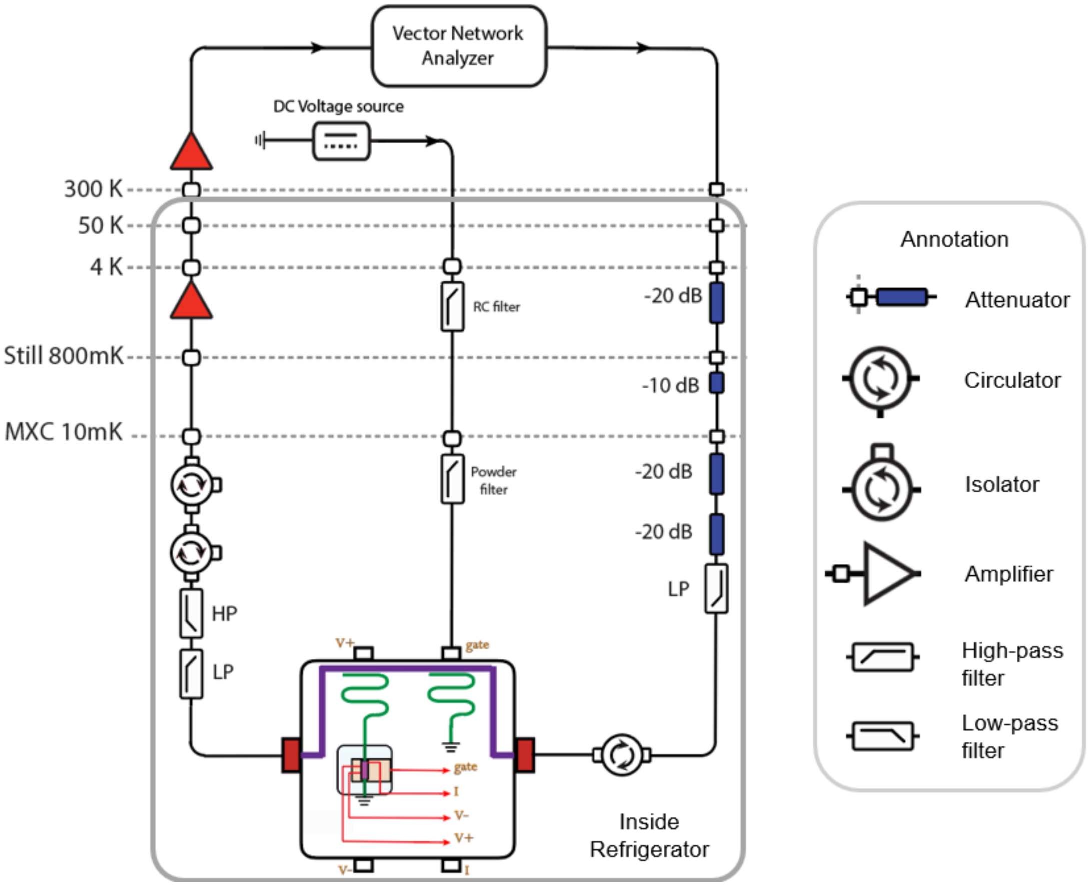

Figure 4-12: Diagram of the microwave measurement setup. The microwave lines connect the chip with the vector network analyzer outside the dilution fridge to apply and read out microwave pulse signals. Along the microwave line, there are filters, circulators, isolators, attenuators and amplifiers mounted at different stages of the fridge.

The microwave characterization setup consists of an Agilent vector network analyzer to apply input microwave signal and readout the response signal and a Yokogawa GS200 DC source to apply gate voltage (similar to the DC measurement setup).

Chapter 5

Measurements and Results

In the first measurement round, we performed the transport characterization and microwave characterization on five different twisted bilayer graphene device packages. The experiment demonstrates that our design of on-chip hybrid DC-microwave circuits is robust as a probe to characterize microwave properties of twisted bilayer graphene devices. Preliminary results also show that we encounter two main fabrication problems:

- The planar contacts fabricated by selectively etching away the top hBN and depositing Al exhibited extremely high resistivity in four devices, which disables the DC four-probe measurement on these devices.
- The twist angle relaxed to a smaller value (0.42^o) than the first magic angle (1.1^o), which caused the absence of superconducting states.

In this chapter, we describe in detail these results along with their implication and limitation.

5.1 Transport characterization

The transport characterization results in this section are from the only device in our first measurement round that has reliable Al-graphene contacts. We apply an AC

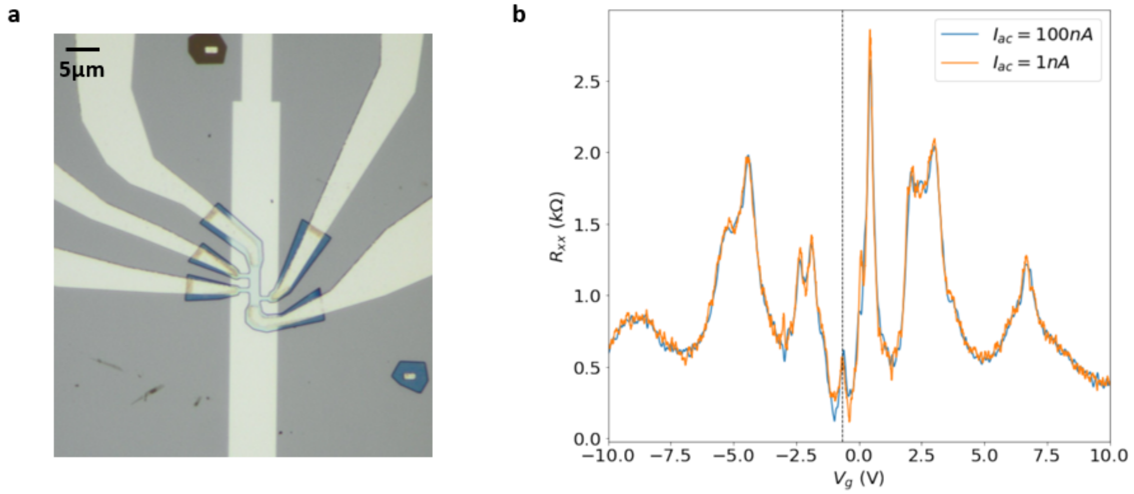

Figure 5-1: **a)** Optical image of the measured device. **b)** Four-probe resistance R_{xx} as a function of applied backgate voltage V_g at two different values of lock-in current bias $I_{ac} = 1$ nA and $I_{ac} = 100$ nA in a twisted bilayer graphene device. The peak at the vertical black dashed line corresponds to the charge neutral point, $V_{CNP} = -0.628$ V. The two traces are almost overlapped and the vanishing of the resistance is not observed at any gate voltage, which suggests the absence of superconducting states in this device.

current bias of 100 nA by setting the lock-in output voltage to 200 mV and choosing $R_{\text{ac bias}} = 2$ MΩ.

We first measure the device resistance R_{xx} as a function of gate voltage at zero DC current bias. The appearance of a small resistance peak at -0.628 V, along with other peak features lying symmetrically on the two sides of that peak, suggest that the gate voltage corresponding to the charge neutrality point (CNP) is -0.628 V. Hence, the charge carrier density is calculated to be:

$$n = \frac{C_g(V_g - V_{CNP})}{e} = \frac{\epsilon_{BN}\epsilon_0(V_g - V_{CNP})}{ed}, \tag{5.1}$$

where V_g is the applied gate voltage, V_{CNP} is the gate voltage corresponding to the charge neutrality point (CNP), $\epsilon_{BN} = 3.76$ is the dielectric constant of hBN [47], and $d = 60$ nm is the thickness of bottom hBN flake measured by AFM. Fig 5-2 shows the device resistance R_{xx} as a function of the charge carrier density and the DC current bias.

We observe that the first hole-like and electron-like resistance peaks, corresponding to possible insulating states, happen around the charge carrier density of 0.43×10^{-12} cm^{-2}, much smaller than the half-filling charge carrier density $(1.2 - 1.6 \times 10^{-12}\ \mathrm{cm}^{-2})$ or the full-filling charge carrier density $(2.4 - 3.2 \times 10^{-12}\ \mathrm{cm}^{-2})$ of MATBG [2], which suggests that the twist angle in our device is not close to the first magic angle value. However, the insulating states happening at such a small carrier density still suggests that there might be the existence of low-energy band gaps in this device. Previous experiments have shown that at the second magic twist angle of 0.45^o, multiple bands are formed and superlattice-induced insulating states happen at integer band fillings, i.e. the corresponding charge carrier density is an integer multiple of superlattice carrier density [48]. Indeed, if we use a twist angle of 0.42^o and $n_s = 8\theta^2/(a^2\sqrt{3}) \approx 0.41 \times 10^{12}\ \mathrm{cm}^{-2}$, the insulating states of our devices happen near integer filling factors $n/n_s = \pm 1, \pm 3$. A more conclusive measurement to confirm whether these peaks corresponding to the full-filled bands is to measure their Landau fans, which we plan to perform in another dilution refrigerator since the current one does not have the capability to provide a magnetic field.

Noticeably, unlike previously reported superconductor-graphene-superconductor junctions [45, 46], even at zero DC current bias, the resistance peaks of our device are weak but non-vanishing, which suggests that the proximitized effect at aluminum-graphene contacts is not strong enough to dominate the intrinsic transport response of the twisted bilayer graphene device. Such a weak proximitized effect is preferable in our case, as we want to investigate the intrinsic superconductivity of twisted bilayer graphene. We conclude that the current geometry of the twisted bilayer graphene device and contacts are suitable to be used in future devices.

In this device, we do not observe any vanishing of R_{xx}. To exclude the possibility of 100 nA current bias being larger than the critical current of intrinsic superconductivity in the device, we repeat the same measurement with zero DC current bias and 1 nA AC current bias provided by the lock-in, which is smaller than the reported critical current of MATBG [4]. We observe a similar plot of R_{xx} as the function of charge carrier density. The result suggests that there is an absence of superconductivity in

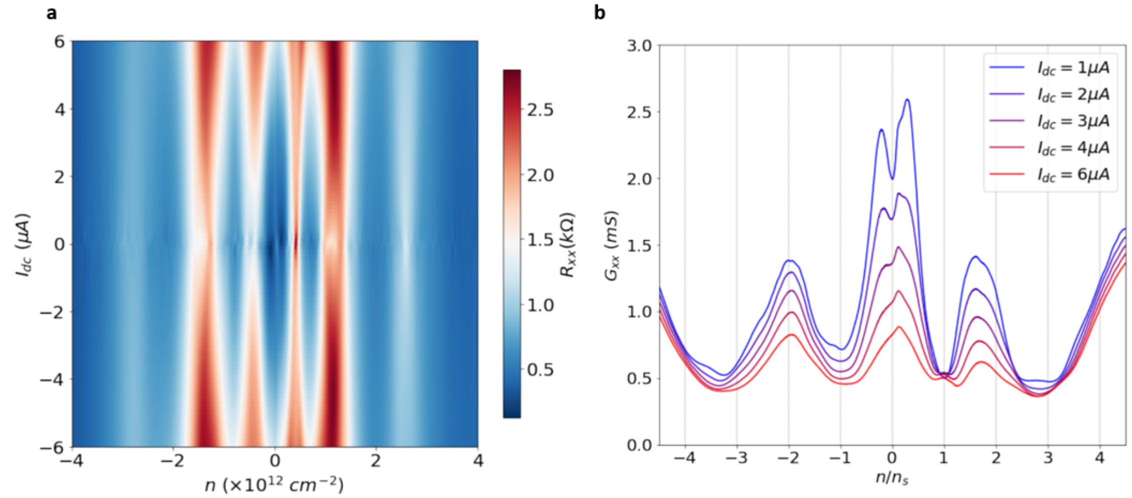

Figure 5-2: **a)** The dependence of the four-probe resistance R_{xx} as a function of DC current bias I_{dc} and charge carrier density n. **b)** The dependence of device conductance G_{xx} at different DC current bias as the function of the filling factor n/n_s, $n_s \approx 0.41 \times 10^{12}$ cm^{-2} is the superlattice density calculated for the twist angle $\theta = 0.42^o$, near the second magic angle. The insulating states (minimal conductance) correspond to the integer filling factors $\pm 1, \pm 3$. The result suggests the twist angle is relaxed during the fabrication process to near $\theta \approx 0.42^o$.

this small-angle-twisted bilayer graphene device, which further confirms the deviation of the twist angle from the first magic angle value.

In the other four devices, the measured contact resistance is on the order of tens of MOhm, which is very large compared to the typical resistance of graphene device. Therefore, we cannot perform the DC characterization on these devices.

5.2 Microwave characterization

At zero gate voltage, we perform a standard VNA measurement, where we apply a microwave tone in the frequency range 3 − 12 GHz to the transmission line and measure its transmission response as the function of frequency. In this coarse scan, we identify the positions of certain sharp peaks above the noise background.

As expected, there is a sharp resonance peak near 6 GHz, the simulated resonance frequency of the control resonator. A finer VNA scan with power -60 dBm from 6.06 GHz to 6.07 GHz is implemented to extract the resonance frequency and

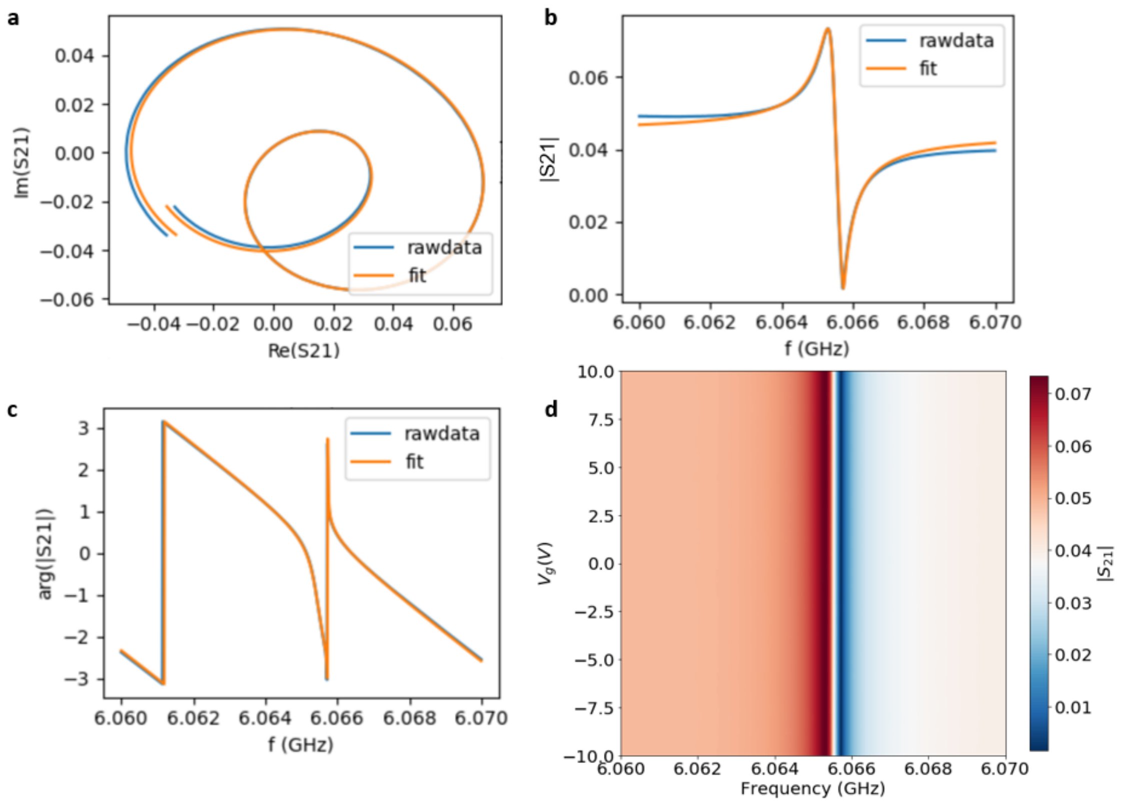

Figure 5-3: **a-c)** Fitting of the resonance peak $f_0 = 6.065$ GHz. **d)** The VNA traces around the resonance peak f_0 does not change with the applied backgate voltage, which confirms that this peak originates from the control resonator.

quality factor. Again, using the resonator tool mentioned in section 4.1, we obtain the fitting results: control resonance frequency $f_0 = 6.065$ GHz and quality factors $Q_{i0} = 245{,}376$, $Q_{c0} = 8{,}623$. We can see that the resonance frequency agrees well with the simulated value for the control resonator in 4.1.1. The internal and coupling quality factors are smaller than the simulated results, which is because the real circuit is subject to surface loss. Furthermore, we repeatedly measure the same VNA scan while the backgate voltage varies between $V_g = -10$ V to $V_g = 10$ V. The independence of the resonance signal's amplitude from the backgate voltage confirms that this peak indeed originates from the control resonator.

We also observe another resonance peak near 4.23 GHz. We perform a finer VNA scan with power -60 dBm from 4.20 GHz to 4.27 GHz while changing the backgate voltage between -10 V and 10 V. A clear change of the peak amplitude with the backgate voltage is shown, which confirms that this peak originates from the experiment resonator with twisted bilayer graphene attached at its end. The resonance peak is significantly broadened compared to the control resonance peak. We again obtain the fitting results: the experiment resonance frequency $f_r = 4.235$ GHz and quality factors $Q_{ir} = 517.5$ and $Q_{cr} = 465.8$. The low internal quality factor of the experiment resonator agrees with the broadening of resonance peak, and is due to the finite resistance (on the order of kΩ) of the twisted bilayer graphene device. Compared to the simulated resonance frequency $f_{r(sim)} = 5.35$ GHz from section 4.1.1, there is a frequency shift due to the contribution of the twisted bilayer graphene device's inductance to the total inductance. We can estimate the inductance contribution L_g from the twisted bilayer graphene device from the shifted resonance frequency.

Using the lumped-element circuit model of the resonator, we have,

$$\frac{f_r}{f_{r(sim)}} = \left(\frac{L'}{L' + L_g}\right)^{1/2} \tag{5.2}$$

where $L' = (8l/\pi^2)L_r$ is the equivalent lumped inductance of the resonator. Thus we estimate $L_g^{\square} \approx 0.15$ nH/$\square$ (given that the geometry of our device is 3 μm $\times 1$ μm). Since $L_g^{\square}$ is much larger than the geometric inductance per square of the device (on the order of 10^{-6} nH/$\square$), $L_g^{\square}$ mainly arises from the kinetic inductance of the twisted bilayer graphene. However, this result is not an estimation of the kinetic inductance of the superconducting state but the kinetic inductance of the high-carrier-mobility conducting state in the twisted bilayer graphene. Nevertheless, the calculation demonstrates how the inductance of the device is extracted in our experimental method.

In addition, we keep the frequency of VNA signal at the resonance frequency $f_r = 4.235$ GHz and measure the transmission response S_{21} while varying the backgate voltage. We notice that the magnitude of the dip at this resonance frequency has local maximum points that nearly coincide with the insulating states measured in DC characterization (Fig 5-5). Since the magnitude of the resonance dip is closely related to the internal quality factor of the resonator, this coincidence suggests a

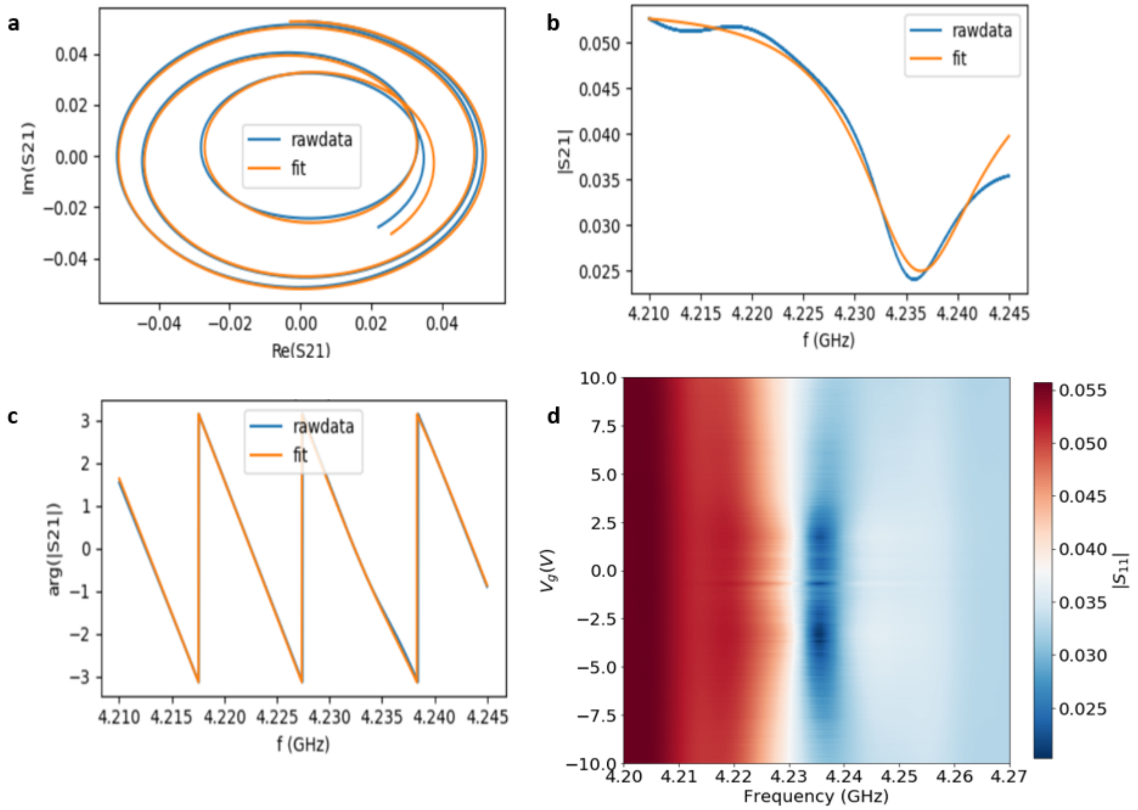

Figure 5-4: **a)** Fitting of the resonance peak $f_r = 4.235$ GHz. **b)** The VNA traces around the resonance peak f_r changes with the applied backgate voltage, which confirms that this peak originates from the experiment resonator attached to the twisted bilayer graphene device.

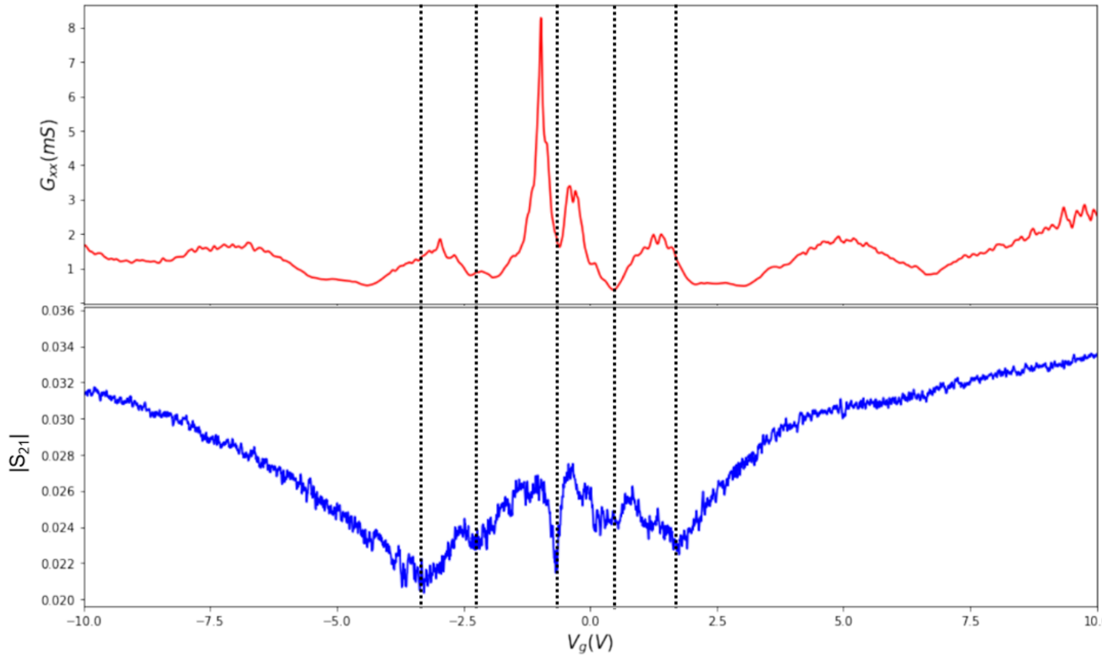

Figure 5-5: The transmission response $|S_{21}|$ as the function of backgate voltage at fixed frequency $f_r = 4.235$ GHz. The local minimum of $|S_{21}|$ corresponds to a local maximum of the resonance dip's magnitude. These local maximum points coincide with the insulating states measured in DC characterization, which suggests a correlation between internal quality factor of the resonator and the conductance of the device.

correlation between the internal quality factor of the resonator and the conductance of the device. Thus, this resonator readout circuit is a promising sensitive and non-invasive probe for the material's phases. However, reproducing this measurement in more twisted bilayer graphene devices would be required to derive a more concrete correlation.

Chapter 6

Conclusion and Outlook

In this thesis, we introduced an experimental method that utilizes a hybrid on-chip DC-microwave circuit to characterize both the transport and high-frequency microwave response of twisted bilayer graphene devices. The transport characterization and microwave characterization in one small-angle twisted bilayer graphene device demonstrate the robustness of this experimental method.

The four-probe transport characterization shows superlattice-induced insulating states and allows us to derive, based on those states, the twist angle of the device at 0.42^o, close to the second magic-angle value. We also find out that the proximitized superconductivity at the aluminum-graphene contacts is so weak that the intrinsic transport response of twisted bilayer graphene device can be measured, even at zero DC current bias. Therefore, the geometry of our fabricated twisted bilayer graphene and contacts are suitable to be used in future devices.

The resonance frequency shift of the experiment resonator coupled to the twisted bilayer graphene is successfully measured with microwave characterization. The result allows us to extract the contribution of twisted bilayer graphene's inductance to the total inductance of the resonator. Moreover, we observe the correlation between the internal quality factor of the resonator and the conductance of the twisted bilayer graphene. Although the measurements on more devices are required to derive a concrete relation, this result suggests that the resonator readout circuit is a promising sensitive probe for the material's inductance and phases in a non-invasive manner.

The relaxation of twist angle in our measured device and the large contact resistance measured in the other four devices limited our first measurement round. Nevertheless, this thesis has laid the foundation for the ongoing project of the MATBG characterization using microwave techniques, which will continue after my graduation. Further investigations with improved control of twist angles and contacts would pave a path to measure the MATBG kinetic inductace and will hopefully be an important step forward to realize MATBG-based superconducting qubit circuits in the near future.

Bibliography

[1] Moon, P. & Koshino, M. Energy spectrum and quantum Hall effect in twisted bilayer graphene. *Physical Review B* **85**, 195458 (2012). URL `https://link.aps.org/doi/10.1103/PhysRevB.85.195458`.

[2] Cao, Y. *et al.* Correlated insulator behaviour at half-filling in magic-angle graphene superlattices. *Nature* **556**, 80–84 (2018). URL `https://www.nature.com/articles/nature26154`.

[3] Bistritzer, R. & MacDonald, A. H. Moiré bands in twisted double-layer graphene. *Proceedings of the National Academy of Sciences* **108**, 12233–12237 (2011). URL `https://www.pnas.org/content/108/30/12233`.

[4] Cao, Y. *et al.* Unconventional superconductivity in magic-angle graphene superlattices. *Nature* **556**, 43–50 (2018). URL `https://www.nature.com/articles/nature26160`.

[5] Balents, L., Dean, C. R., Efetov, D. K. & Young, A. F. Superconductivity and strong correlations in moiré flat bands. *Nature Physics* **16**, 725–733 (2020). URL `https://www.nature.com/articles/s41567-020-0906-9`.

[6] Song, C. *Microwave Properties of Vortices in Superconducting Resonators*. Ph.D., Syracuse University, United States – New York (2011). URL `https://www.proquest.com/docview/922419273/abstract/8BEFE014EBBE4AE9PQ/1`.

[7] Gao, J. *The Physics of Superconducting Microwave Resonators*. Ph.D., California Institute of Technology, United States – California (2008). URL `https://www.proquest.com/docview/1080814168/abstract/9B4D25A9432846EBPQ/1`.

[8] Mazin, B. A. *Microwave kinetic inductance detectors*. Ph.D., California Institute of Technology, United States – California (2005). URL `https://www.proquest.com/docview/305005058/abstract/794775436CD54552PQ/1`.

[9] Kjaergaard, M. *et al.* Superconducting Qubits: Current State of Play. *Annual Review of Condensed Matter Physics* **11**, 369–395 (2020). URL `https://doi.org/10.1146/annurev-conmatphys-031119-050605`.

[10] Devoret, M. H. & Schoelkopf, R. J. Superconducting Circuits for Quantum Information: An Outlook. *Science* **339**, 1169–1174 (2013). URL `https://science.sciencemag.org/content/339/6124/1169`.

[11] Devoret, M. H., Wallraff, A. & Martinis, J. M. Superconducting Qubits: A Short Review. *arXiv:cond-mat/0411174* (2004). URL `http://arxiv.org/abs/cond-mat/0411174`. ArXiv: cond-mat/0411174.

[12] Novoselov, K. S. *et al.* Electric Field Effect in Atomically Thin Carbon Films. *Science* **306**, 666–669 (2004). URL `https://science.sciencemag.org/content/306/5696/666`.

[13] Ajayan, P., Kim, P. & Banerjee, K. Two-dimensional van der Waals materials. *Physics Today* **69**, 38–44 (2016). URL `https://physicstoday.scitation.org/doi/full/10.1063/PT.3.3297`.

[14] Wang, L. *et al.* One-Dimensional Electrical Contact to a Two-Dimensional Material. *Science* **342**, 614–617 (2013). URL `https://science.sciencemag.org/content/342/6158/614`.

[15] Wang, J. I.-J. *et al.* Coherent control of a hybrid superconducting circuit made with graphene-based van der Waals heterostructures. *Nature Nanotechnology* **14**, 120–125 (2019). URL `https://www.nature.com/articles/s41565-018-0329-2`.

[16] Walsh, E. D. *et al.* Josephson junction infrared single-photon detector. *Science* **372**, 409–412 (2021). URL `https://science.sciencemag.org/content/372/6540/409`.

[17] Lee, G.-H. *et al.* Graphene-based Josephson junction microwave bolometer. *Nature* **586**, 42–46 (2020). URL `https://www.nature.com/articles/s41586-020-2752-4`.

[18] Yamoah, M. *et al.* Microwave dielectric loss of hexagonal Boron Nitride in the low-temperature, single-photon regime P11.006 (2019). URL `http://adsabs.harvard.edu/abs/2019APS..MARP11006Y`.

[19] Rodan-Legrain, D. *et al.* Highly tunable junctions and non-local Josephson effect in magic-angle graphene tunnelling devices. *Nature Nanotechnology* 1–7 (2021). URL `https://www.nature.com/articles/s41565-021-00894-4`. Publisher: Nature Publishing Group.

[20] Andrei, E. Y. & MacDonald, A. H. Graphene bilayers with a twist. *Nature Materials* **19**, 1265–1275 (2020). URL `https://www.nature.com/articles/s41563-020-00840-0`.

[21] Yankowitz, M. *et al.* Tuning superconductivity in twisted bilayer graphene. *Science* **363**, 1059–1064 (2019). URL `https://science.sciencemag.org/content/363/6431/1059`.

[22] Nuckolls, K. P. *et al.* Strongly correlated Chern insulators in magic-angle twisted bilayer graphene. *Nature* **588**, 610–615 (2020). URL `https://www.nature.com/articles/s41586-020-3028-8`.

[23] Wong, D. *et al.* Cascade of electronic transitions in magic-angle twisted bilayer graphene. *Nature* **582**, 198–202 (2020). URL https://www.nature.com/articles/s41586-020-2339-0.

[24] Tinkham, M. *Introduction to superconductivity* (2015). OCLC: 962022037.

[25] Prozorov, R. & Giannetta, R. W. Magnetic penetration depth in unconventional superconductors. *Superconductor Science and Technology* **19**, R41–R67 (2006). URL https://doi.org/10.1088/0953-2048/19/8/r01.

[26] Hardy, W. N., Bonn, D. A., Liang, R., Kamal, S. & Zhang, K. Microwave Penetration Depth Measurements as a Probe of the Superconducting State of YBCO. In Yamafuji, K. & Morishita, T. (eds.) *Advances in Superconductivity VII*, 191–196 (Springer Japan, Tokyo, 1995).

[27] Glover, R. E. & Tinkham, M. Conductivity of Superconducting Films for Photon Energies between 0.3 and $40kT_c$. *Physical Review* **108**, 243–256 (1957). URL https://link.aps.org/doi/10.1103/PhysRev.108.243.

[28] Glover, R. E. & Tinkham, M. Transmission of Superconducting Films at Millimeter-Microwave and Far Infrared Frequencies. *Physical Review* **104**, 844–845 (1956). URL https://link.aps.org/doi/10.1103/PhysRev.104.844.

[29] Casparis, L. *et al.* Superconducting gatemon qubit based on a proximitized two-dimensional electron gas. *Nature Nanotechnology* **13**, 915–919 (2018). URL https://www.nature.com/articles/s41565-018-0207-y.

[30] Nguyen, L. B. Toward the Fluxonium Quantum Processor (2020). URL https://drum.lib.umd.edu/handle/1903/26545.

[31] Brooks, P., Kitaev, A. & Preskill, J. Protected gates for superconducting qubits. *Physical Review A* **87**, 052306 (2013). URL https://link.aps.org/doi/10.1103/PhysRevA.87.052306.

[32] Yuan, N. F. Q. & Fu, L. Model for the metal-insulator transition in graphene superlattices and beyond. *Physical Review B* **98**, 045103 (2018). URL https://link.aps.org/doi/10.1103/PhysRevB.98.045103.

[33] Cao, Y. *et al.* Superlattice-Induced Insulating States and Valley-Protected Orbits in Twisted Bilayer Graphene. *Physical Review Letters* **117**, 116804 (2016). URL https://link.aps.org/doi/10.1103/PhysRevLett.117.116804.

[34] Xu, C. & Balents, L. Topological Superconductivity in Twisted Multilayer Graphene. *Physical Review Letters* **121**, 087001 (2018). URL https://link.aps.org/doi/10.1103/PhysRevLett.121.087001.

[35] Isobe, H., Yuan, N. F. & Fu, L. Unconventional Superconductivity and Density Waves in Twisted Bilayer Graphene. *Physical Review X* **8**, 041041 (2018). URL https://link.aps.org/doi/10.1103/PhysRevX.8.041041.

[36] Guo, H., Zhu, X., Feng, S. & Scalettar, R. T. Pairing symmetry of interacting fermions on a twisted bilayer graphene superlattice. *Physical Review B* **97**, 235453 (2018). URL `https://link.aps.org/doi/10.1103/PhysRevB.97.235453`.

[37] Ochi, M., Koshino, M. & Kuroki, K. Possible correlated insulating states in magic-angle twisted bilayer graphene under strongly competing interactions. *Physical Review B* **98**, 081102 (2018). URL `https://link.aps.org/doi/10.1103/PhysRevB.98.081102`.

[38] Laksono, E. *et al.* Singlet superconductivity enhanced by charge order in nested twisted bilayer graphene Fermi surfaces. *Solid State Communications* **282**, 38–44 (2018). URL `https://www.sciencedirect.com/science/article/pii/S0038109818304903`.

[39] Mohan, S., del Mar Hershenson, M., Boyd, S. & Lee, T. Simple accurate expressions for planar spiral inductances. *IEEE Journal of Solid-State Circuits* **34**, 1419–1424 (1999). Conference Name: IEEE Journal of Solid-State Circuits.

[40] Grünhaupt, L. *et al.* Granular aluminium as a superconducting material for high-impedance quantum circuits. *Nature Materials* **18**, 816–819 (2019). URL `https://www.nature.com/articles/s41563-019-0350-3`.

[41] Microwave Engineering, 4th Edition | Wiley. URL `https://www.wiley.com/en-us/Microwave+Engineering%2C+4th+Edition-p-9780470631553`.

[42] Göppl, M. *et al.* Coplanar waveguide resonators for circuit quantum electrodynamics. *Journal of Applied Physics* **104**, 113904 (2008). URL `http://aip.scitation.org/doi/10.1063/1.3010859`.

[43] Probst, S., Song, F. B., Bushev, P. A., Ustinov, A. V. & Weides, M. Efficient and robust analysis of complex scattering data under noise in microwave resonators. *Review of Scientific Instruments* **86**, 024706 (2015). URL `https://aip.scitation.org/doi/full/10.1063/1.4907935`.

[44] Kim, K. *et al.* van der Waals Heterostructures with High Accuracy Rotational Alignment. *Nano Letters* **16**, 1989–1995 (2016). URL `https://doi.org/10.1021/acs.nanolett.5b05263`. Publisher: American Chemical Society.

[45] Wang, I.-J. Superconducting Proximity Effect in Graphene Nanodevices: A Transport and Tunneling Study (2016). URL `https://dash.harvard.edu/handle/1/26718763`.

[46] Schmidt, F. E., Jenkins, M. D., Watanabe, K., Taniguchi, T. & Steele, G. A. A ballistic graphene superconducting microwave circuit. *Nature Communications* **9**, 4069 (2018). URL `https://www.nature.com/articles/s41467-018-06595-2`.

[47] Laturia, A., Van de Put, M. L. & Vandenberghe, W. G. Dielectric properties of hexagonal boron nitride and transition metal dichalcogenides: from monolayer to bulk. *npj 2D Materials and Applications* **2**, 1–7 (2018). URL `https://www.nature.com/articles/s41699-018-0050-x`.

[48] Lu, X. *et al.* Multiple Flat Bands and Topological Hofstadter Butterfly in Twisted Bilayer Graphene Close to the Second Magic Angle. *arXiv:2006.13963 [cond-mat]* (2020). URL `http://arxiv.org/abs/2006.13963`. ArXiv: 2006.13963.